



Contents lists available at ScienceDirect

International Journal of Mining Science and Technology

journal homepage: www.elsevier.com/locate/ijmst

Multistage hydraulic fracturing of a horizontal well for hard roof related coal burst control: Insights from numerical modelling to field application

Jiaxin Zhuang^{a,b}, Zonglong Mu^{a,b,*}, Wu Cai^{a,c,*}, Hu He^d, Lee J. Hosking^e, Guojun Xi^f, Biao Jiao^f^aJiangsu Engineering Laboratory of Mine Earthquake Monitoring and Prevention, Xuzhou 221116, China^bSchool of Mines, China University of Mining and Technology, Xuzhou 221116, China^cState Key Laboratory for Fine Exploration and Intelligent Development of Coal Resources, Xuzhou 221116, China^dSchool of Resources and Geosciences, China University of Mining and Technology, Xuzhou 221116, China^eDepartment of Civil and Environmental Engineering, Brunel University London, Uxbridge, Middlesex UB8 3PH, UK^fShaanxi Binchang Huijiahe Mining Company Limited, Xianyang 713602, China

ARTICLE INFO

Article history:

Received 23 June 2024

Received in revised form 17 August 2024

Accepted 25 August 2024

Available online 21 September 2024

Keywords:

Coal burst

Multistage hydraulic fracturing of horizontal wells

Mining-induced seismicity

Mining-induced stress

Effectiveness evaluation

ABSTRACT

Multistage hydraulic fracturing of horizontal wells (MFHW) is a promising technology for controlling coal burst caused by thick and hard roofs in China. However, challenges remain regarding the MFHW control mechanism of coal burst and assessment of the associated fracturing effects. In this study, these challenges were investigated through numerical modelling and field applications, based on the actual operating parameters of MFHW for hard roofs in a Chinese coal mine. A damage parameter (D) is proposed to assess the degree of hydraulic fracturing in the roof. The mechanisms and effects of MFHW for controlling coal burst are analyzed using microseismic (MS) data and front-abutment stress distribution. Results show that the degree of fracturing can be categorized into lightly-fractured ($D \leq 0.3$), moderately fractured ($0.3 < D \leq 0.6$), well-fractured ($0.6 < D \leq 0.9$), and over-fractured ($0.9 < D \leq 0.95$). A response stage in the fracturing process, characterized by a slowdown in crack development, indicates the transition to a well-fractured condition. After MFHW, the zone range and peak value of the front-abutment stress decrease. Additionally, MS events shift from near the coal seam to the fractured roof layers, with the number of MS events increases while the average MS energy decreases. The MFHW control mechanisms of coal bursts involve mitigating mining-induced stress and reducing seismic activity during longwall retreat, ensuring stresses remain below the ultimate stress level. These findings provide a reference for evaluating MFHW fracturing effects and controlling coal burst disasters in engineering.

© 2024 Published by Elsevier B.V. on behalf of China University of Mining & Technology. This is an open access article under the CC BY-NC-ND license (<http://creativecommons.org/licenses/by-nc-nd/4.0/>).

1. Introduction

Coal burst or rock burst has been one of the most severe dynamic disasters occurring in Chinese coal mines [1]. In 2019, there were 132 coal burst incidents reported in coal mines in China, rising to 319 in 2022 [2]. Rock burst is a dynamic event characterized by the abrupt instability and failure of the surrounding rock and its support structure during longwall retreating and roadway excavation [2,3]. One of the crucial factors inducing coal burst is the hard-thick roof above the coal [4]. Additionally, retention of coal pillars also plays a significant role in triggering coal burst [5]. As the longwall retreats, the area of unsupported hard-thick roof increases, with more elastic energy stored, which increases the abutment stress, potentially exceeding 3–4 times

the overburden stress [6]. Roof failure can then lead to high-energy microseismic (MS) events. Such MS events occur with high-dynamic loading, exerting on the abutment stress (high static stress) and increasing the risk of coal burst [7]. Therefore, preweakening of the hard roof is crucial for coal burst control [8,9]. In the past few years, presplitting blasting, roof cutting blasting, and hydraulic fracturing have been increasingly used in China. However, recently, Multistage hydraulic fracturing of horizontal wells (MFHW) has gained increasing popularity.

Hydraulic fracturing is the process of pumping fluid through the wellbore into rock to stimulate cracks for oil and gas production [10]. MFHW have been extensively exploited for the production of petroleum or gas, leading to the creation of multiple cracks and fracture networks within the stratum [11,12]. Hydraulic fracturing in hard roof strata (Fig. 1) has been proven to be effective in mitigating abutment stresses induced by longwall mining [13]. Using hydraulic fracturing on the base roof can reduce stress peaks

* Corresponding authors.

E-mail addresses: muzonglong@163.com (Z. Mu), caiwu@cumt.edu.cn (W. Cai).

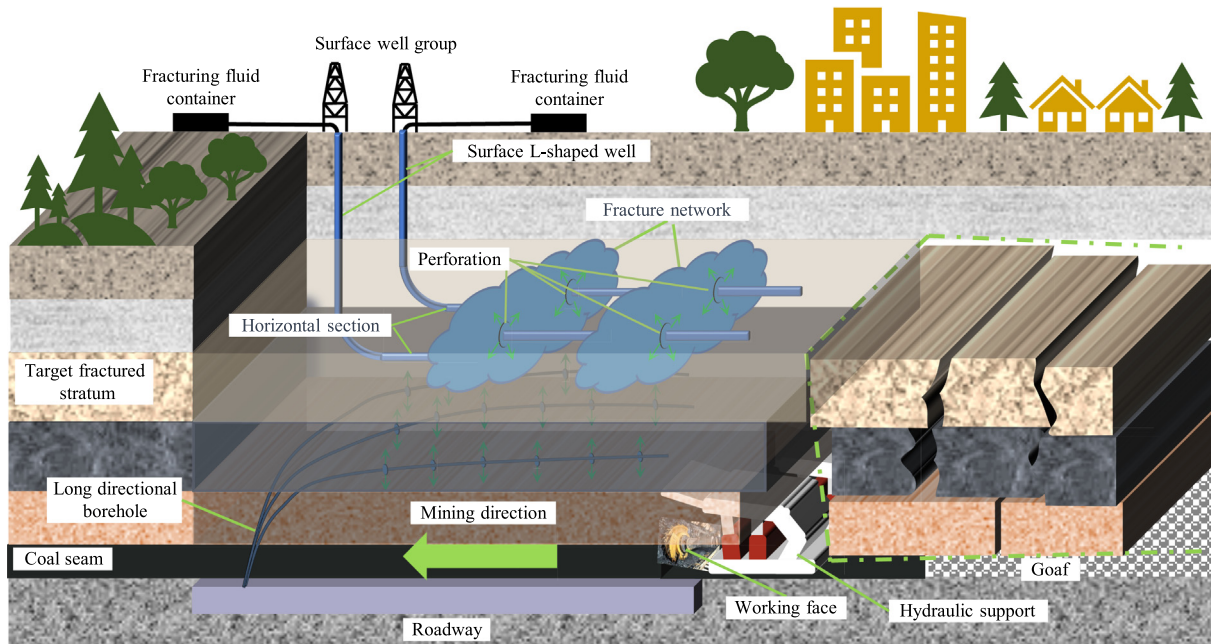


Fig. 1. Schematic illustration of multistage hydraulic fracturing of horizontal wells (MFHW).

and shift them deeper into the coal wall. This changes the breakage structure of rock strata, reduces the initial rupture distance of the hard roof, and can even facilitate the extremely thick and hard rock to move in layers [14,15]. To be specific, it could reduce the periodic roof weighting interval, minimize prolonged periodic roof weighting, and eliminate dynamic loading and mining-induced seismicity due to massive roof rupture. During the process of longwall mining, the total number of MS events increases, but the number of high-energy MS events decreases, compared to the scenarios of non-fractured hard roof [16]. In addition, it can alleviate the response of support resistance in the working face and control roadway deformation [17]. The target fracturing strata can be determined based on the rock mechanics parameters, thickness, and distance from the coal seam of the roof strata [18]. Balancing the tensile stress zones and induced stress between cracks is essential to determine appropriate fracture spacing, avoiding the inefficiencies of too-small spacing that hinder fracture initiation and expansion, and preventing the safety risks of too-large spacing that can compromise the stope [19]. The evaluation of the effectiveness of hydraulic fracturing in the target fracturing zone is often based on the distribution of MS data [20].

The findings from previous studies have elucidated that the MFHW could promote hard roof strata caving, reduce abutment pressure, and mitigate high-energy MS events. However, the MFHW control mechanisms of coal burst and assessment of the associated fracturing effects remain unclear. Specifically, there is a lack of detailed methodologies for assessing the extent of roof fracturing, understanding how varying degrees of fracturing influence the evolution of MS events and abutment stress, and determining the corresponding effectiveness in coal burst prevention. This exploration is crucial for providing a foundation for the rational selection of fracturing strategies. Using the Hujiahe Coal Mine in China as a case study, this research established a large-scale UDEC model based on the mine's geological conditions, reproducing the process by which fracturing can reduce mining-induced stress and high-energy seismic events, and analyzing the MFHW control mechanisms of coal burst. Different fracturing scenarios were investigated under varying injection volumes, and the degree of fracturing was calculated based on damage parameters.

This provided a method for evaluating the fracturing effectiveness during the MFHW process. By analyzing patterns of MS events and stress changes, the study assessed the effectiveness of MFHW in coal burst prevention, establishing a method for evaluating control effectiveness and demonstrating a significant reduction in the risk of coal burst after implementing MFHW in field practice.

2. Methodology

2.1. Prototype description

The Hujiahe coal mine is located in Shaanxi Province, China. The mining field stretches 8.1 km from east to west and 6.5 km from north to south. The current longwall mining operation is in the No. 4 coal seam as shown in the mining plan in Fig. 2, which has a burial depth of 680 m with a dip angle of less than 5° and an average recoverable thickness of 13.5 m. On the northern side of the 401106 longwall panel, it is the 401105 longwall face (the first mining panel of the mining district), which has been mined. To the west is the protective coal pillar of the 401 mining district, while to the east is the sedimentary structure formed by river erosion. DF5 is a reverse fault, which trends NE-NE and strikes NW-N, with a dip angle of 45° and a throw ranging from 0 to 15 m. It extends approximately 1454 m in this mining panel district.

Around the 401106 longwall panel, there are three drill holes (B1, B2, and B3) located from west to east. The distribution of various rock layers within 100 m above the coal seam was analyzed at these drill holes. The roof stratum above the coal seam primarily consists of high-strength sandstone (Fig. 3). At drill hole B1, there is a 36.1 m thick medium sandstone situated 6.5 m above the coal seam. Additionally, there are coarse sandstone layers with thicknesses of 13.8 and 13.4 m, located 42.6 and 92.4 m above the coal seam, respectively. At drill hole B2, there is a 14.5 m-thick coarse sandstone layer at 53.9 m, a 17.1 m-thick medium-grained sandstone layer at 68.4 m, and a 24.3 m-thick siltstone layer at 85.5 m above the coal seam. At drill hole B3, there are two fine sandstone layers with thicknesses of 23.1 and 14.5 m, located 29.5 and 72 m above the coal seam, respectively. Additionally, there are sandy mudstone layers, 18 and 21 m thick, situated 11.5 and

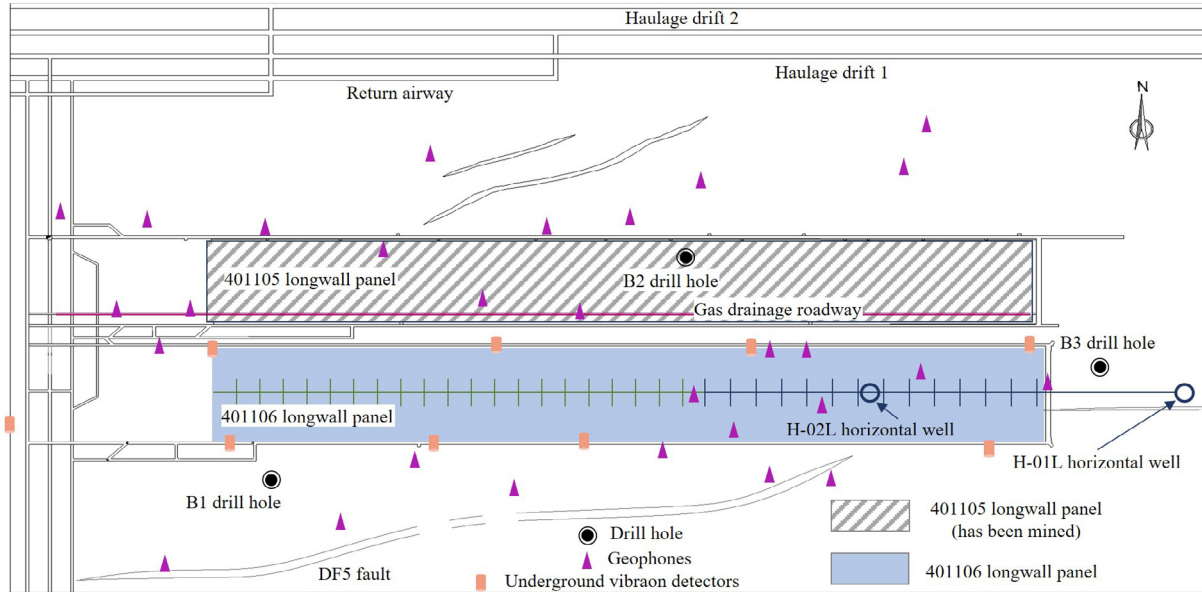


Fig. 2. Geological map of the Hujiahe coal mine.

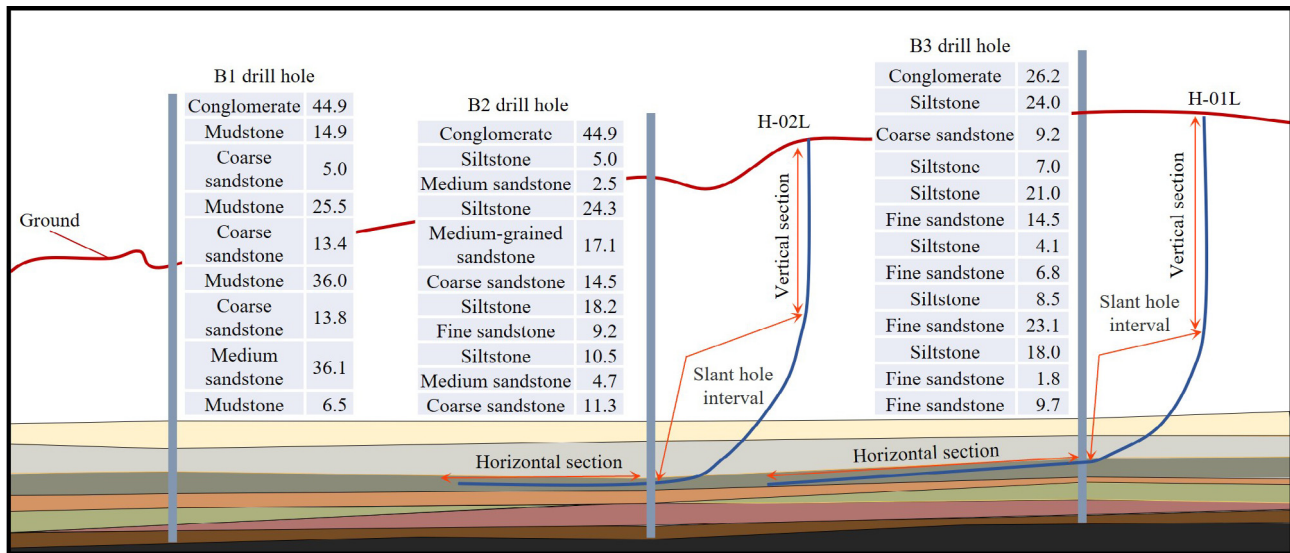


Fig. 3. MFHW deployed in the 401,106 longwall panel. Lithological distribution characteristics of boreholes B1, B2, and B3.

86.5 m above the coal seam, respectively. The uniaxial compressive strengths of these strata range from 73.3 to 85.3 MPa for siltstone, 55.7 to 69.8 MPa for fine sandstone, 11.7 to 16.3 MPa for coarse sandstone, 18.2 to 23.8 MPa for sandy mudstone, and 49.2 to 78.3 MPa for medium sandstone. Under such multi-layer thick and hard roof stratum conditions, the roof is less susceptible to caving during longwall panel retreat. This results in suspended strata in the goaf and stress concentration ahead of the longwall face, increasing the risk of coal burst. Based on the comprehensive analysis of boreholes B1, B2, and B3, it is observed that there is a sandstone layer with an average thickness of 20 m above the coal seam, within the range of 60–90 m. This sandstone layer is characterized by calcareous cementation, making it a resilient rock layer with good integrity and high strength. When it is broken, it will cause strong activity within surrounding rock, potentially triggering coal burst. Therefore, this is the target stratum for MFHW.

The arrangement of MFHW in longwall 401106 is illustrated in Fig. 3. The H-01L horizontal well is divided into 14 segments, while the H-02L horizontal well is divided into 20 segments. Each segment was designed with 50 m space, but some of them were altered according to the well-logging information. The fracturing operation was carried out with an injection rate of 16.0 m³/min, which produced injection pressures ranging between 19.4 and 23.9 MPa. The relationship between the injection rate and pressure during the fracturing operation in the H-01L well is depicted in Fig. 4.

2.2. Numerical modelling

The discrete element method is a rock mechanics computational approach that has evolved from the theory of discontinuous media [21]. It considers joints or weak planes as controllers of rock

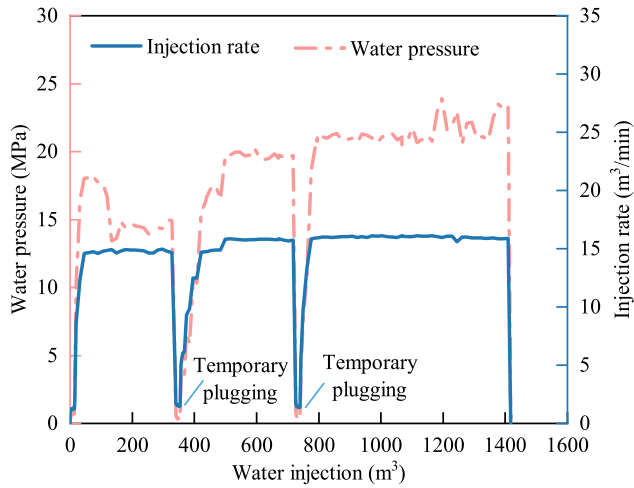


Fig. 4. H-01L hydraulic fracturing construction curves.

mass behavior. In universal distinct element code (UDEC), fluids are stored within virtual pores/cracks formed by unit elements (represented as blocks or particles). In UDEC, blocks are impermeable, and fluid flows only through contacts between blocks (Fig. 5). UDEC performs fully coupled mechanical-hydraulic analysis, where fracture conductivity depends on mechanical deformation, and joint fluid pressures influence mechanical computations. This enables accurate simulation of fluid–structure interactions in fractured media. The corresponding equations for fluid computation in UDEC are Eqs. (1)–(3).

During the MFHW process, water flowing within the contact zone generates significant tensile stresses, which decrease the effective normal stress on the contact. This results in the opening of incipient fractures, which subsequently serve as pathways for hydraulic fracture propagation [22]. Fracture induced by MFHW propagate in the direction where they can most easily open up [23]. The fracture therefore tends to follow the direction of the major principal stress while opening along the direction of minor principal stress.

Fluid pressure at a point of contact is calculated by Eq. (1).

$$F_i = p n_i L \tag{1}$$

where F_i is the contact force per unit length along the contact interface; p the fluid pressure; n_i the normal direction; and L the contact length.

Darcy’s law is applied to describe fluid flow in the contact zone, as shown in Eq. (2)

$$q = -a^3 \frac{k_w (\sum Q \Delta t - \Delta V)}{12 \mu L V} \tag{2}$$

where μ is the dynamic viscosity of the fluid; a the contact hydraulic aperture; L the length assigned to the contact between the domains; $\sum Q \Delta t$ the cumulative fluid volume over time; ΔV the change in volume; K_w the bulk modulus of the fluid; and V the volume.

The representation of the contact aperture as ‘ a ’ is calculated by Eq. (3)

$$a = a_0 + \Delta a \tag{3}$$

where a_0 is the joint aperture at zero normal stress; and Δa the change in contact aperture, decreasing under compression and increasing under tension.

This study utilizes UDEC to establish a large-scale numerical model along the coal seam strike direction, corresponding to the longwall face mining direction shown in Fig. 6, with Hujiahe coal mine as the background.

Through UDEC’s coupled mechanical-hydraulic analysis module, it investigates the stress and MS evolution during coal mining under various fracturing degrees. The numerical model is 260 m long and 130 m wide. MFHW for the target stratum is located 60 m above the coal seam. The target strata were divided into triangles using the UDEC-Trigon model, while other strata were divided into rectangles to simulate the rock blocks formed after mining. A uniform grid with consistent edge length was subsequently generated for all blocks in the model. The blocks were modeled using a Mohr-Coulomb model, while the contact was modeled using the Coulomb slip model [24]. The calibrated [25,26] rock mechanical parameters are shown in Table 1. The in-situ stress measurement shows that the average horizontal stress reached 13.1 MPa and

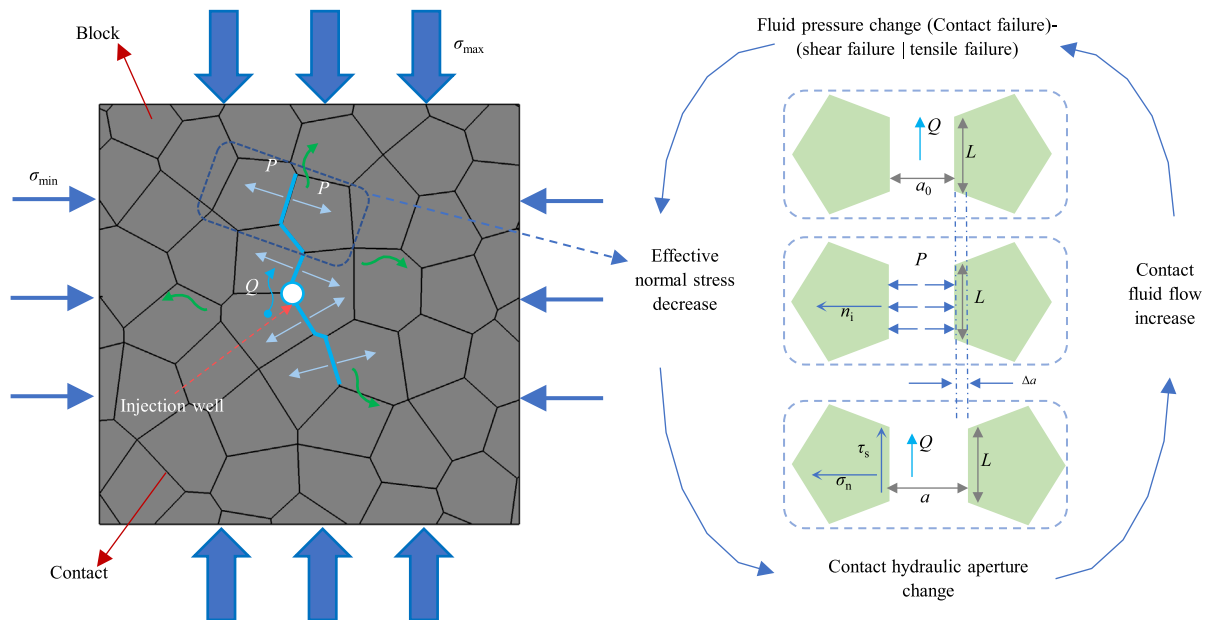


Fig. 5. UDEC hydraulic fracturing crack propagation model (Fluid/solid interaction in discontinua).

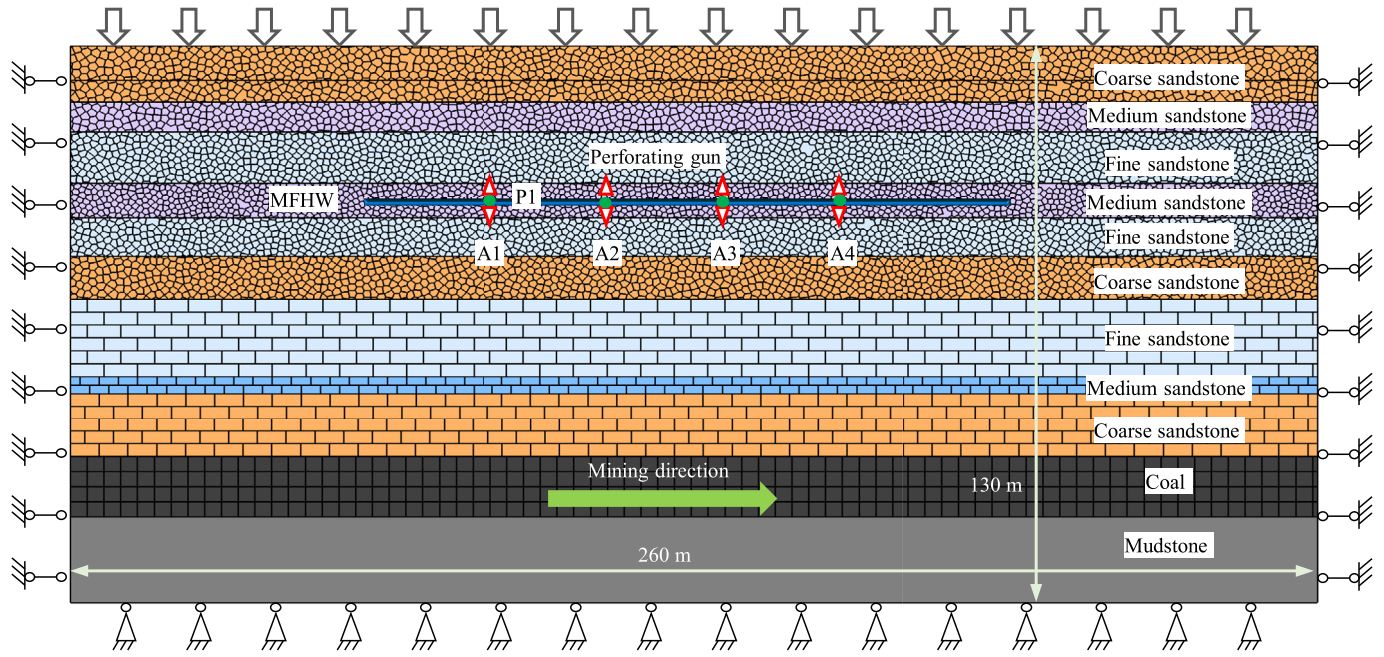


Fig. 6. Numerical simulation of MFHW for a hard roof mining operation.

Table 1
Mechanical parameters of rocks.

Rock strata	Matrix properties					Contact properties			
	Young's modulus E (GPa)	Poisson's ratio	Cohesion (MPa)	Friction (°)	Tensile strength (MPa)	Normal stiffness (GPa/m)	Shear stiffness (GPa/m)	Aperture zero load (m)	Permeability factor (Pa ⁻¹ s ⁻¹)
Coarse sandstone	22.0	0.22	3.60	41.2	1.60	26.9	9.4	0.007	0.25
Fine sandstone	20.0	0.24	4.10	37.7	1.70	56.6	19.8	0.006	0.10
Medium sandstone	23.0	0.20	6.20	28.7	2.10	78.8	27.6	0.005	0.10
Coal	5.0	0.32	0.75	30.0	0.30	9.6	3.4	0.001	0.01
Mudstone	3.8	0.21	5.10	36.0	1.16	58.8	21.2	0.001	0.01

the average vertical stress reached 17.5 MPa in the coal mine. Therefore, an initial horizontal stress of 13.1 MPa and an initial vertical stress of 17.5 MPa were applied to the numerical model. In addition, a vertical stress of 14.4 MPa was applied to the upper boundary considering that the overlying rock layers were not fully included in the model.

The flowchart of numerical modeling is depicted in Fig. 7. First, the material properties are defined, and then the horizontal displacements of the left and right boundaries of the model, as well as the vertical position of the bottom boundary, are fixed. In addition, an equivalent vertical stress was applied to the upper boundary, considering that the overlying rock layers were not fully included in the model. Afterward, the number of fracturing segments is determined, and water injection is conducted at a constant flow rate in corresponding positions in the MFHW. Next, monitor the changes in water pressure at the injection point. During water injection, information on contacts within the model, such as total fracture length, total fracture number, and total fracture aperture is recorded using the FISH function in UDEC. This function iterates through all contact information, assesses whether the joints have failed (in tension or shear), and if so, records the corresponding contact information.

Subsequently, changes in zone strain energy (MS) during the longwall retreat process and variations in front-abutment pressure peak are recorded. To calculate MS energy, first, function 1 loops through all zones stored in the model's temporary storage, known as 'model extras', and records the zone's xx-stress, yy-stress, xy-

stress, and corresponding strains. The strain energy of each zone is calculated by multiplying the stress and strain values. Function 2 then continues looping to assess the current state of each block using the Mohr-Coulomb failure criterion. If a zone experiences failure, the zone's coordinates, xx-stress, yy-stress, xy-stress, and strain at that moment are recorded, followed by calculation of the strain energy. The model extras store the state of the model at the previous timestep, and the strain energy calculated from the model extra variables is subtracted from the strain energy of the zone undergoing failure at the current timestep to obtain the released energy, which represents the MS energy. Finally, MS events are exported using the table function in UDEC and used to analyze the evolution patterns of MS. The methodology for calculating zone store energy and the corresponding formula is given by Eq. (4).

$$U_z = \sigma_{xx}\epsilon_{xx} + \sigma_{xy}\epsilon_{xy} + \sigma_{yy}\epsilon_{yy} \tag{4}$$

where U_z is zone store energy; σ_{xx} , σ_{xy} and σ_{yy} the zone stress components (normal and shear stresses); and ϵ_{xx} , ϵ_{xy} and ϵ_{yy} the zone strain components corresponding to the stress components.

3. Results and analyses

3.1. Hydraulic fracturing process

Based on the use of MFHW for hard roof construction parameters of the Hujiahe coal mine, the numerical model adopts an injec-

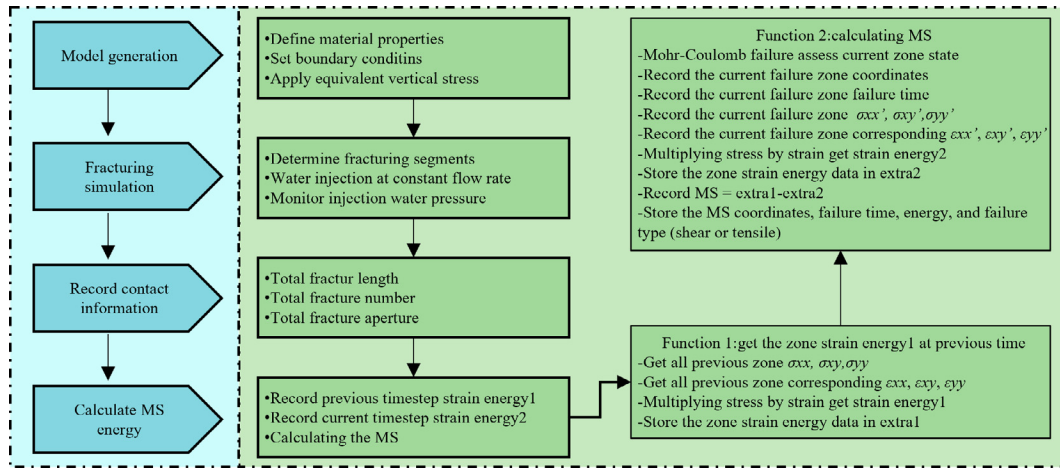


Fig. 7. Flowchart of the numerical modelling process adopted in this work.

tion rate of 16 m³/min for the fracturing stratum. We assume the boundary conditions are of the Neumann type, where an injection rate of 16 m³/min is applied. Initially, water injection at positions A1 and A2 is conducted. Subsequently, water injection at positions A3 and A4 is performed. The spacing between A1, A2, A3, and A4 measures 50 m each. Fig. 8 depicts the variation of water pressure and the expansion of fractures during the development of the MFHW. As the water flows, the water pressure around the perforation begins to uniformly disperse and increase. This article analyzes the variation in water pressure under water injections of 400, 800, 1200, and 1600 m³, corresponding to Scenarios 1, 2, 3, and 4, respectively. The injection rates are consistent across all scenarios, but the total injected volume varies. In Scenario 1, the water pressure increases from 0 to 21 MPa, resulting in the creation of a high-pressure zone (dashed-line area) with a 20 m vertical impact range (Fig. 8a). The fracture induced by MFHW propagates and develops along the direction of the maximum principal stress (sig1), reaching a length of 16 m (Fig. 8b). In Scenario 2, water pressure rises from 0 to 22.5 MPa, expanding the high-pressure zone (dashed-line area) to a 30 m vertical impact range (Fig. 8c). The length of the resulting hydraulic fracturing-induced fracture increases to 27 m (Fig. 8d). The Scenario 3, water pressure climbs from 0 to 23 MPa, further extending the high-pressure zone (dashed-line area) to a 40 m vertical impact range (Fig. 8e). Consequently, the hydraulic fracturing-induced fracture length reaches 40 m (Fig. 8f). In Scenario 4, the water pressure increases from 0 to 23.5 MPa, covering a 50 m vertical impact range within the high-pressure zone (dashed-line area) (Fig. 8g). Consequently, the corresponding hydraulic fracturing-induced fracture length reaches 45 m (Fig. 8h).

3.2. Characterization of fracturing effect

During the water injection in MFHW for hard roofs, MS can be detected. MS data can effectively assess the fracturing effect and range [20,27]. This study employed the FISH function to perform a real-time analysis of fracture development induced by the MFHW injection process. The FISH function continuously monitors all contacts within the numerical model. When a contact's normal stress reaches zero, or when shear failure occurs according to the Mohr-Coulomb criterion, the function automatically counts and records the corresponding fracture's length and aperture. These values are continuously accumulated throughout the simulation, providing comprehensive data on the development of fractures. This approach allows for a detailed and dynamic record of the fracture count, length, and aperture induced by the MFHW injection pro-

cess. Cai et al. [28] defined the damage parameter and established a relationship between cumulative damage and the degree of damage. In this context, a hydraulic fracturing-induced fracture damage parameter D was defined, as shown in Eq. (5).

$$D = 1 - \exp(-c_f/c_F) \tag{5}$$

$$c_F = -\max\{c_f\} / \ln\{1 - D_F\}$$

where c_f could be the cumulative count, aperture, and length of fractures induced by hydraulic fracturing, respectively. The average value of c_f , denoted as c_F , can be determined by assuming that the critical damage $D_F=0.95$ corresponds to the maximum value of cumulative hydraulic fracturing-induced fractures (count, aperture, and length).

Damage parameters were calculated based on the cumulative number of fractures, cumulative length, and cumulative aperture during the water injection process, as shown in Fig. 9. We have defined four levels of fracturing intensity: lightly-fractured degree ($D \leq 0.3$), moderately fractured degree ($0.3 < D \leq 0.6$), well-fractured degree ($0.6 < D \leq 0.9$), and over-fractured degree ($0.9 < D \leq 0.95$). The evaluation data corresponding to different levels of roof fracturing are shown in Table 2. Before reaching the well-fractured stage, which includes lightly and moderately fractured stages, both the crack length and quantity show linear growth. When the fracturing degree reaches the well-fractured stage, the crack development rate starts to slow down. As the fracturing degree intensifies to the over-fractured stage, the crack development rate further decreases significantly. The initial slowdown in the crack development rate indicates the transition to the response stage, which signifies that well-fractured has been achieved. This stage occurs at an injected volume of approximately 700 to 1100 m³.

Based on relevant research on MS damage reconstruction [28], we can assess the degree of fracturing. Based on the MS data detected during the fracturing in the target stratum in the H-01L and H-02L horizontal wells of Hujiahe coal mine, we calculated the damage parameters corresponding to the fracturing stratum, which led to the generation of the damage pattern shown in Fig. 10. The area enclosed by the innermost contour line indicates a damage parameter of approximately 0.9, suggesting that the rock strata in this area have been well-fractured. The white area in the figure indicates that the rock strata in this area have experienced lightly fractured.

During MFHW, MS responses were monitored jointly from the surface and underground. Statistical analysis of MS data was collected during the fracturing stages in H-01L stages 5, 6, 8, 9, and 12. The analysis revealed the relationship between the height, length, and width of fractures generated during the MFHW. It also

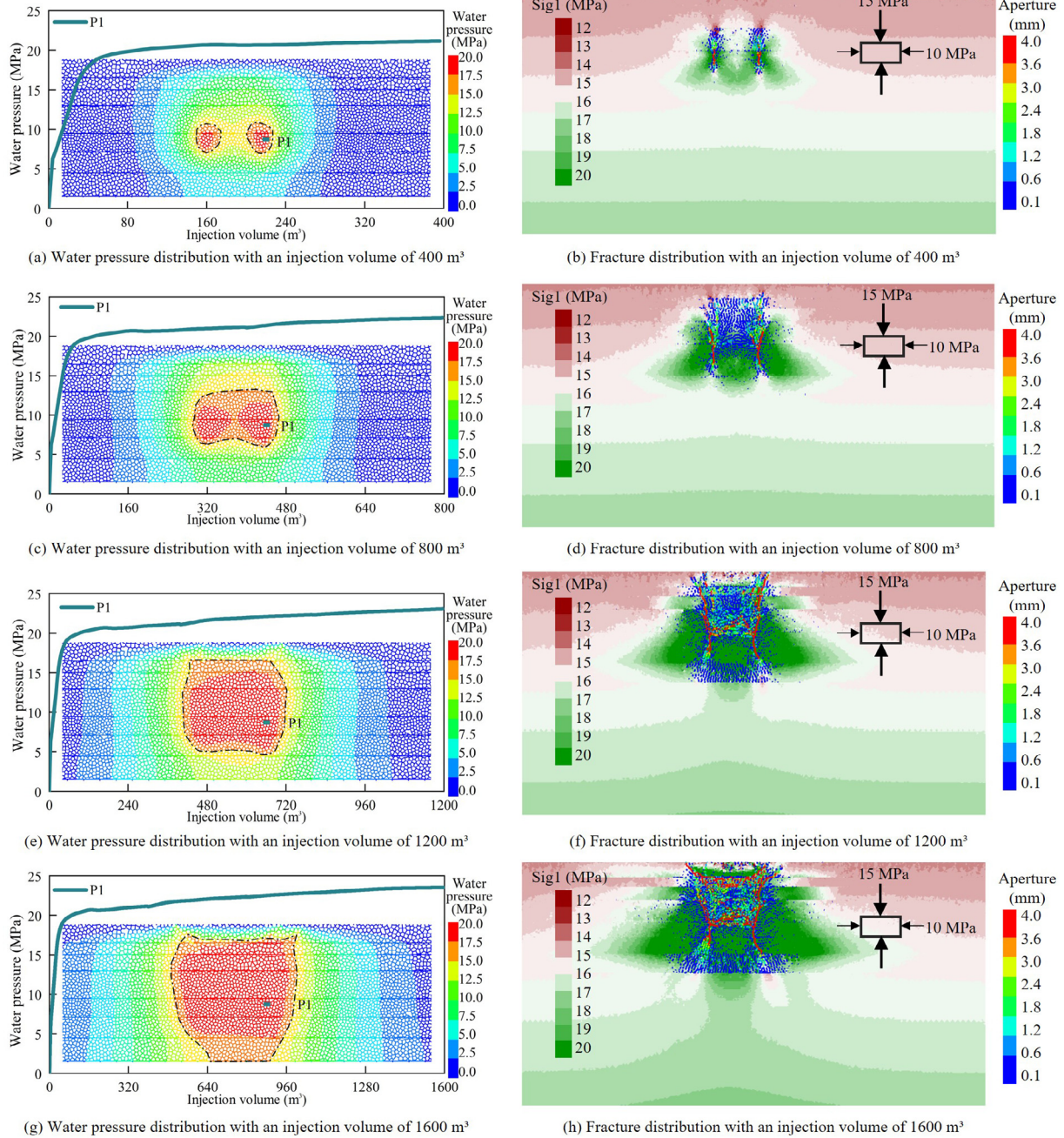


Fig. 8. Pore pressure diffusion and fracture development in MFHW.

showed the relationship between these fractures and the volume of fracturing fluid injected, as shown in Fig. 11. The length of fractures increased linearly as the volume of water increased. However, after approximately 1000 m³ of water, the rate of increase in fracture length with increasing fluid volume became significantly slower. The relationship between water injection and fracture structure suggests that the target strata were not sufficiently fractured before reaching the inflection point in fluid volume. As water injection increased, the fracture gradually intensified as a result. After reaching the inflection point, the target strata became well-fractured, after which the rate of fracture development decreased.

Fig. 12 illustrates the evolution of water pressure and the *D*-value from both numerical simulations and field measurements. Under the same water injection rate, the evolution of water pres-

sure simulated numerically aligns closely with the actual measured water pressure observed in the field (Fig. 12a). As the volume of injected fluid increases, the *D*-value evolution calculated from fracture parameters in the numerical simulation shows a strong consistency with the *D*-value calculated from MS events monitored on-site (Fig. 12b). To quantify this relationship, we calculated the Pearson correlation coefficient (*r*), which measures the linear correlation between two datasets. The Pearson correlation coefficient is calculated by Eq. (6).

$$r = \frac{\sum(x_i - \bar{x})(y_i - \bar{y})}{\sqrt{\sum(x_i - \bar{x})^2 \sum(y_i - \bar{y})^2}} \quad (6)$$

where *x_i* and *y_i* are the individual data points from the two datasets (numerical simulation and field applications, respectively); \bar{x} the

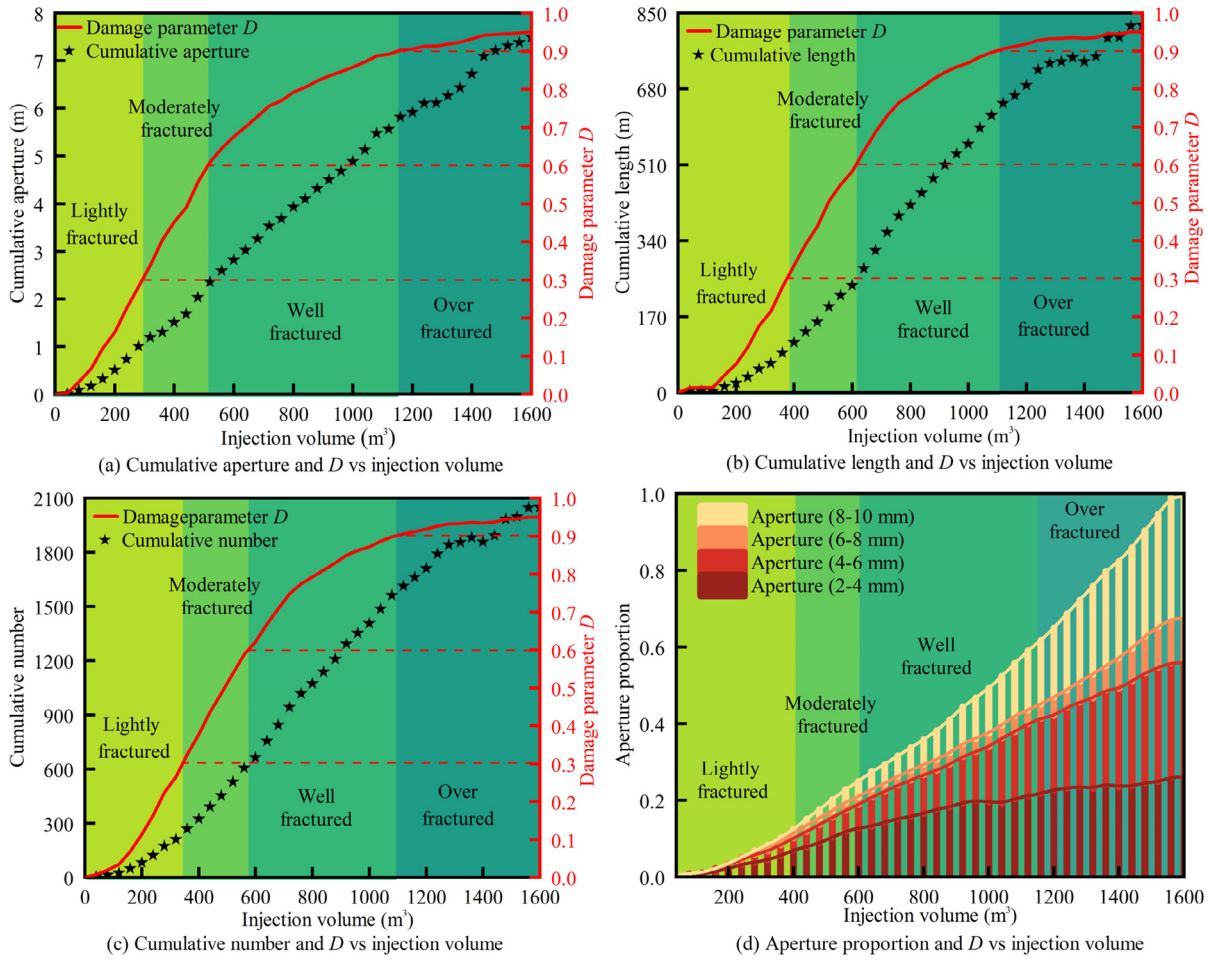


Fig. 9. The relationship between fracturing degree and injection volume. Note: Fracturing degree indicated by shading intensity: Lightly fractured, moderately fractured, well fractured, and over fractured.

Table 2
MFHW effectiveness assessment expressed in terms of selected parameters.

Degree of rock fracturing	Total fracture aperture (m)	Total fracture length (m)	Total fracture count	Injection volume (m ³)	Damage parameter
Lightly fractured	2.4	302	730	300	0.0–0.3
Moderately fractured	4.8	605	1446	520	0.3–0.6
Well-fractured	7.2	901	2169	1150	0.6–0.9
Over-fractured	7.6	950	2290	1600	0.9–0.95

mean of the values (numerical simulation data); and \bar{y} the mean of the values (field measurement data).

The Pearson correlation coefficient between these two sets of D -values is 0.94, indicating a high degree of correlation (Fig. 12c). This strong correlation indicates that the numerical simulation results align well with field application data, thereby validating the reliability of the model [29].

3.3. Fracturing effect on mining-induced stress

After hydraulic fracturing at points A1, A2, A3, and A4 in the sandstone stratum, an artificial fracture zone dominated by four primary vertical fractures is illustrated in Fig. 13.

Fig. 14 illustrates the distribution of yy -stress, xx -stress, and xy -stress in the model under different fracturing conditions as the longwall face retreats 60 m. Without MFHW for the sandstone

layer, it is evident that during the longwall retreat, the overhanging structure of the sandstone layer leads to increased yy -stress ahead of the working face. In the cases without fractured, lightly-fractured, and well-fractured, the affected area of the yy -stress concentration zone (Fig. 14a, b, and c) in front of the longwall face ranges from 32, 21 to 5 m respectively. The yy -stress peak ahead of the working face diminishes from 27.2, 25.4 to 21.7 MPa. The xx -stress (horizontal stress) of the target fracturing stratum is approximately 17 MPa. The stress concentration zones, marked by the dashed-lines in Fig. 14d, e, and f, cover ranges of 50, 40, and 34 m, respectively. As fracturing becomes more thorough, the degree of weakening in the rock stratum increases. Therefore, the stress concentration zones formed become more dispersed, resulting in a smaller impact area. The xy -stress (shear stress) of the target fracturing stratum is approximately 7 MPa. The stress concentration zones, depicted in magenta in Fig. 14g, h, and i, have ranges

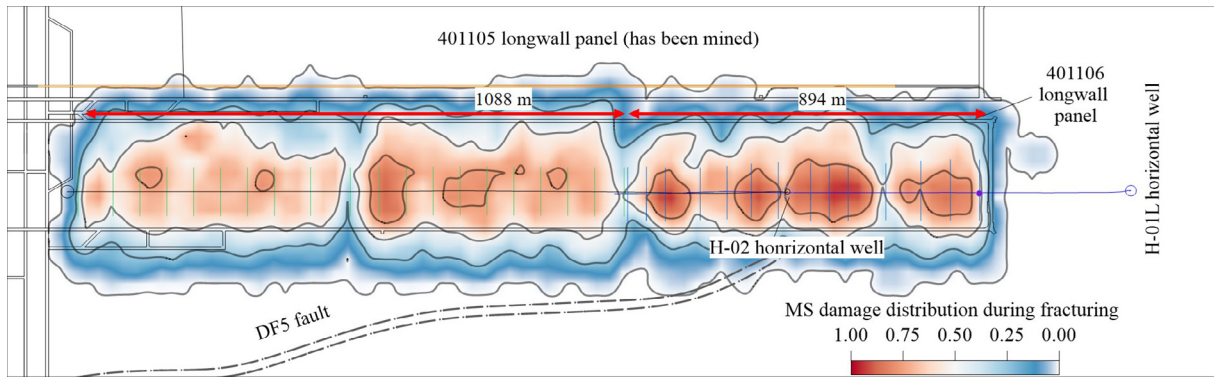


Fig. 10. The distribution of MFHW MS damage.

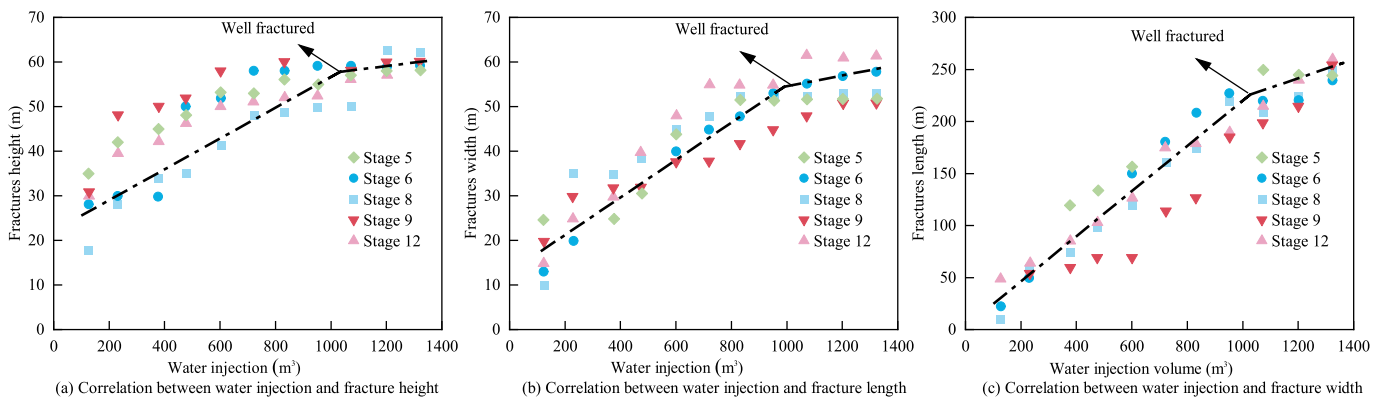


Fig. 11. Liquid injection and MS response.

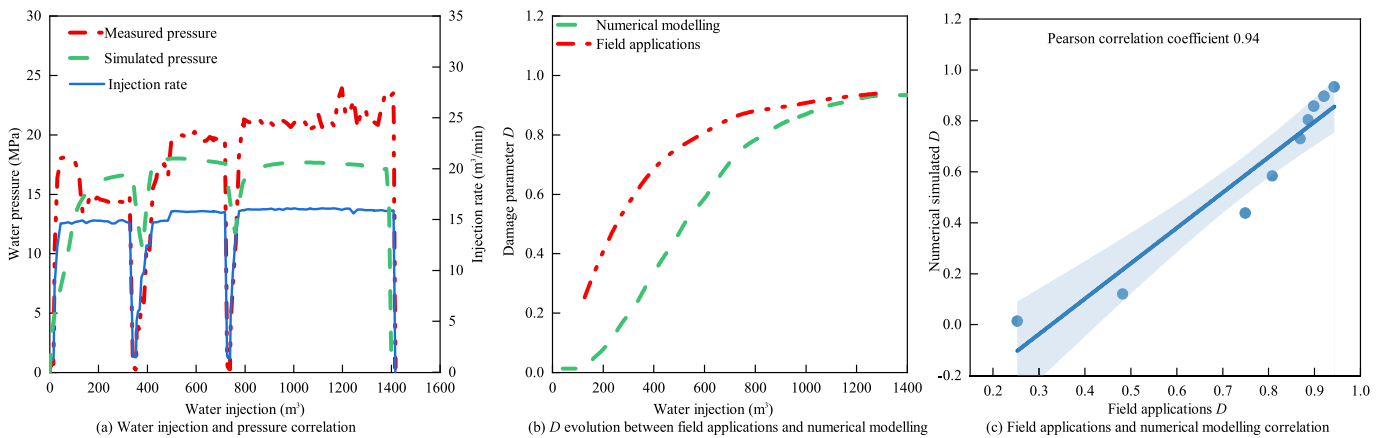


Fig. 12. Pressure and D evolution between numerical simulations and field applications.

of 38, 29, and 15 m respectively. As the fracturing becomes more thorough, the stress concentration zones formed become smaller and shift deeper away from the longwall face.

Fig. 15 illustrates the vertical stress distribution within the model as the longwall face retreats to 90 and 120 m under different fracturing conditions. In the case of unfractured conditions, peak stresses at the longwall face reach 27.5 and 26.5 MPa at 90 m and 120 m retreats, respectively, with associated front-abutment influence ranges of 69 and 64 m. The lightly fractured hard roof promotes the controlled release, reducing the front-abutment pressure peak to 25.7 and 24.5 MPa at the same retreat distances.

Correspondingly, the influence ranges decrease to 55 and 49 m, respectively. In the well-fractured condition, the front-abutment pressure peaks further decline to 23.4 and 22.7 MPa at 90 and 120 m retreats, respectively, with corresponding influence ranges diminish to 35 and 32 m.

It can be observed that application of MFHW in the sandstone stratum reduces both the front-abutment pressure peak and the front-abutment pressure zone, based on the comprehensive analysis of Figs. 14 and 15. During the longwall retreat to 120 m, Fig. 16 illustrates the characteristics of the front abutment distribution under three different fracturing conditions. In the case without

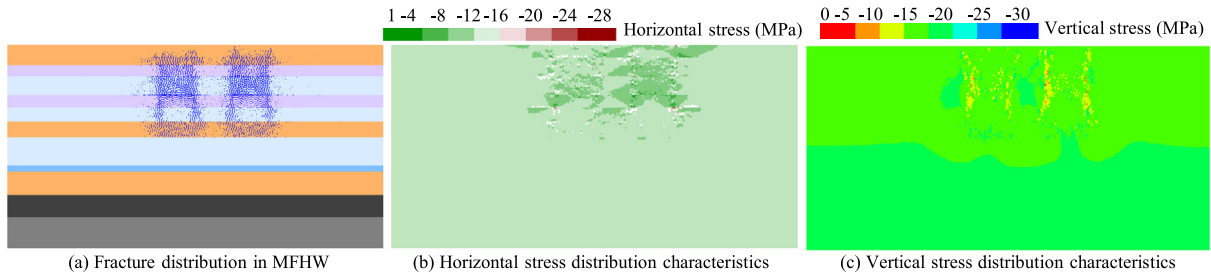


Fig. 13. The effective MFHW for the hard roof.

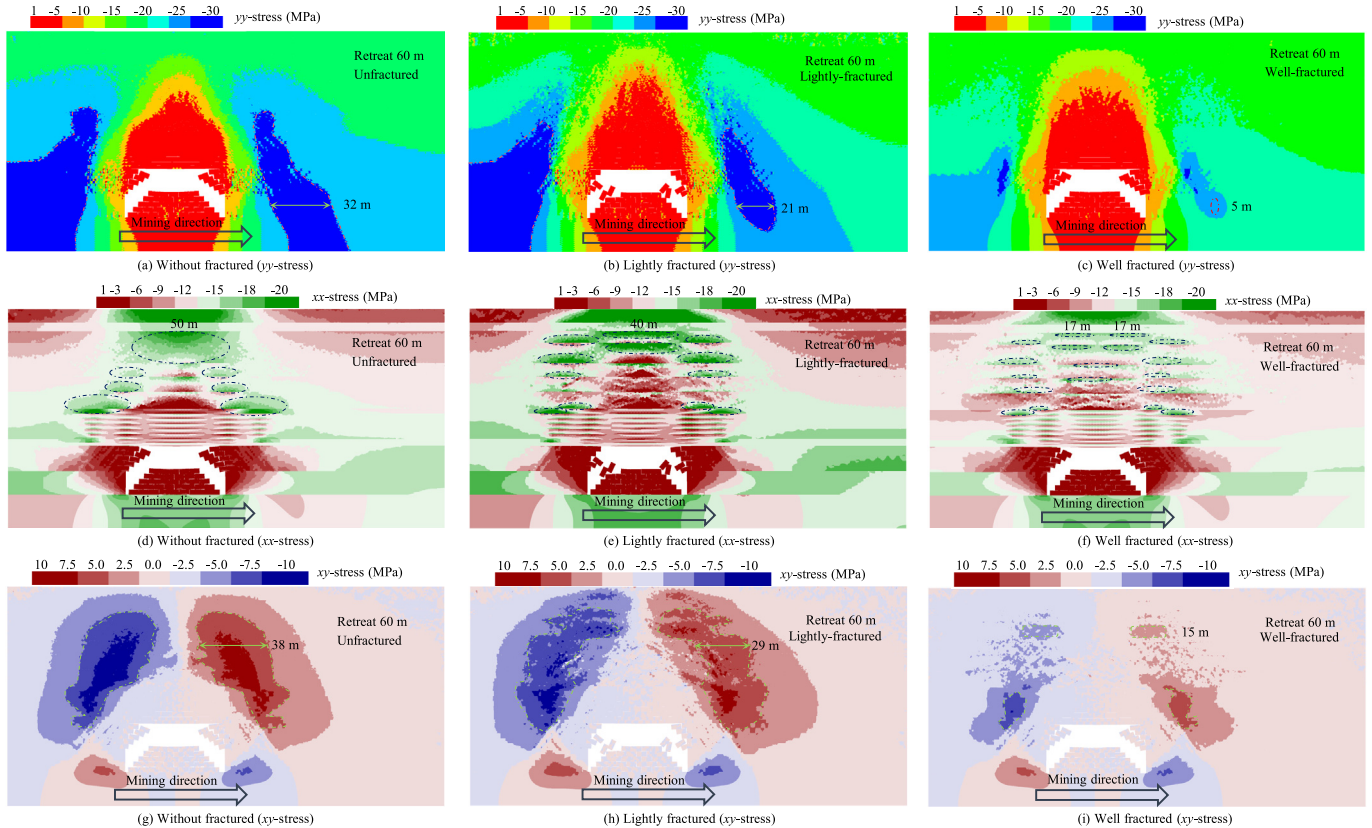


Fig. 14. Stress distribution in the model.

fractured, the advance stress peak is 26.5 MPa. For the lightly fractured case, the abutment stress peak decreases to 24.5 MPa, and for the well-fractured case, the abutment stress peak further reduces to 22.7 MPa. These findings show that after MFHW process, the front-abutment pressure is significantly reduced, indicating a decrease in mining-induced stress on the coal seam. This stress reduction is beneficial for coal burst control, highlighting the effectiveness of MFHW in mitigating mining-induced hazards.

3.4. Fracturing effect on mining-induced seismicity

During the longwall face retreat process, the FISH function in UDEC was used to statistically analyze the strain energy differential generated by zone failure. The differential was subsequently utilized as the MS energy, illustrated in Figs. 17 and 18, under different fractured conditions during the longwall face retreat process. Fig. 17a, c, and e illustrate the distribution of MS energy under different conditions of longwall face retreat by 60 m, for

the unfractured, lightly fractured, and well-fractured cases, respectively. Fig. 17b, d, and f depict the longwall face retreat by 90 m.

When comparing Figs. 14 and 15, it is evident that in models without MFHW for hard roofs, MS events of 10^3 J primarily occur within the front-abutment pressure zone of the longwall face. In contrast to the scenario without fractured, the lightly-fractured scenario and well-fractured scenario exhibit a decreasing trend in the occurrence of 10^3 J MS events. Overall, there is an apparent transition of MS activity from higher to lower energy, and this trend becomes more pronounced with increasing levels of fracturing. Fig. 18a, c, and e illustrate the distribution of MS events, with consideration given to the conditions involving unfractured, lightly-fractured, and well-fractured scenarios, as the working face retreats 120 m. Fig. 18b provides an overview of the total energy and frequency of the MS events. Fig. 18d portrays the distribution of MS events in the vertical direction. In comparison to the unfractured conditions, the total mining-induced seismic energy increased during longwall retreats of 120 m. With the lightly-

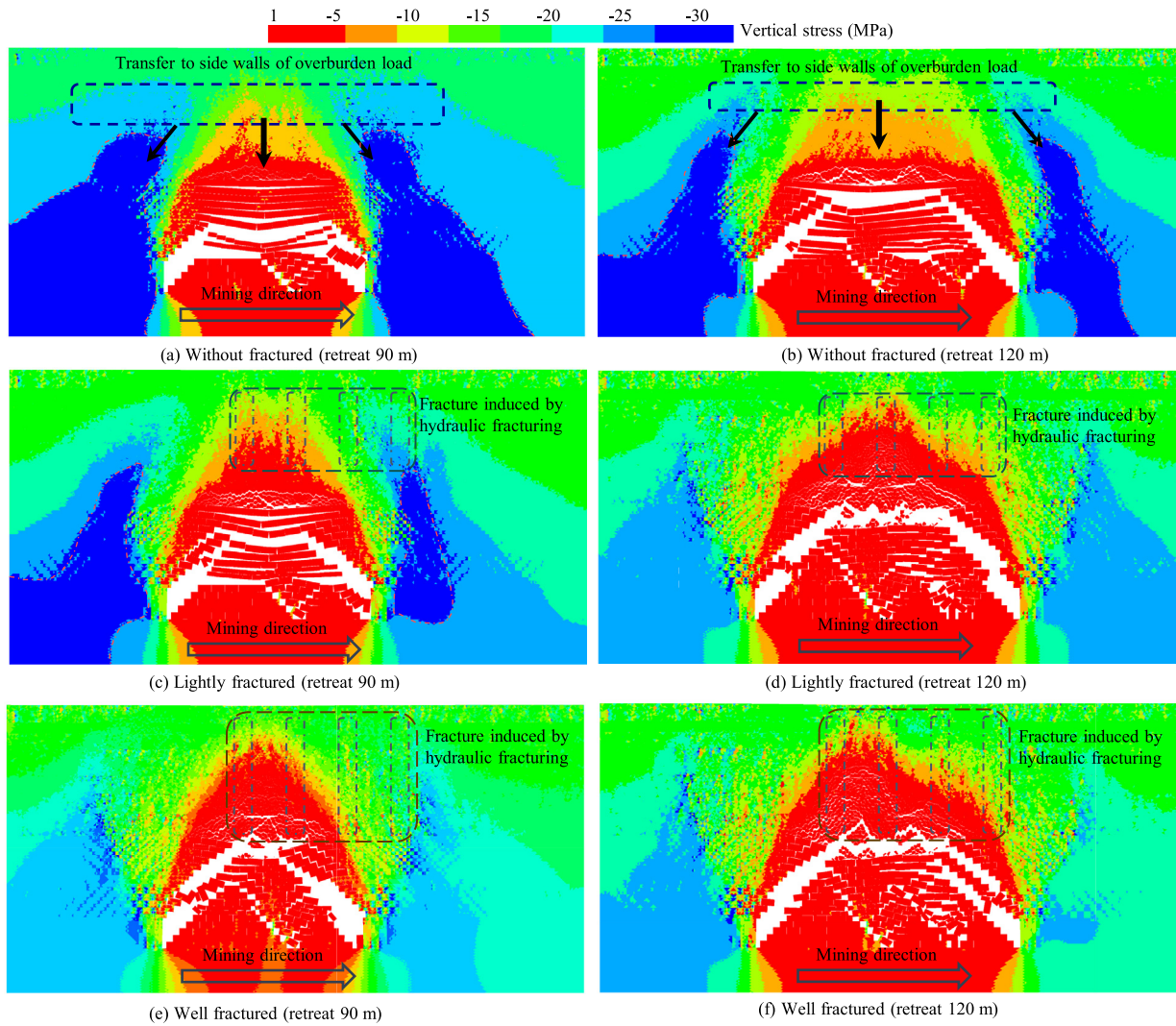


Fig. 15. The evolution of vertical stress with longwall face mining.

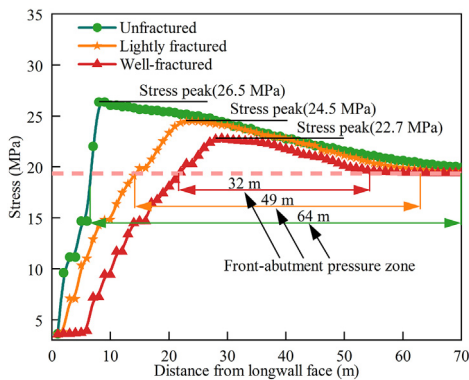


Fig. 16. Front abutment stress peaks and range.

fractured and well-fractured conditions of the total MS energy rose to 801057 and 876004 J, respectively, from the initial 759787 J. Simultaneously, the frequency of occurrences also increased to 1177 and 1385, respectively, from 1012. The average energy per occurrence decreased to 680.6 and 632.5 J, respectively, from 750.7 J.

When the longwall face retreats, MS events exhibited reductions of 27% and 33% for the lightly fractured and well-fractured models, respectively, in the 0–30 m range above the coal seam, compared to the unfractured condition. Both models experienced substantial increases in MS events within the 30–100 m range above the coal seam. In comparison to the unfractured condition, these increases were 88% and 150% for the lightly fractured and well-fractured models, respectively. The MS events with energies of 10 and 1000 J show a decreasing trend, while those with energies of 100 J show an increasing trend. These findings indicate that after fracturing, the average energy of MS events is reduced, and there is a significant decrease in high-energy (1000 J) MS events close to the coal seam. This indicates a reduction in dynamic stress disturbances, which is beneficial for coal burst control.

Fig. 19 and 20 depict the distribution of MS events after the 110 m retreat of the 401106 longwall (post-fractured) and the 401105 longwall (without fractured). During the 110 m retreat of the 401106 and 401105 longwall panels, 629 and 537 MS events were detected in the roof of each longwall, respectively, concentrated within 200 m ahead and 50 m behind the face. With MFHW development, the total energy of MS events in the 401106 longwall was 1145484 J, with an average energy of 1821 J. Without MFHW development, the total energy of MS events in the 401105 longwall was 1042685 J, with an average energy of 1942 J.

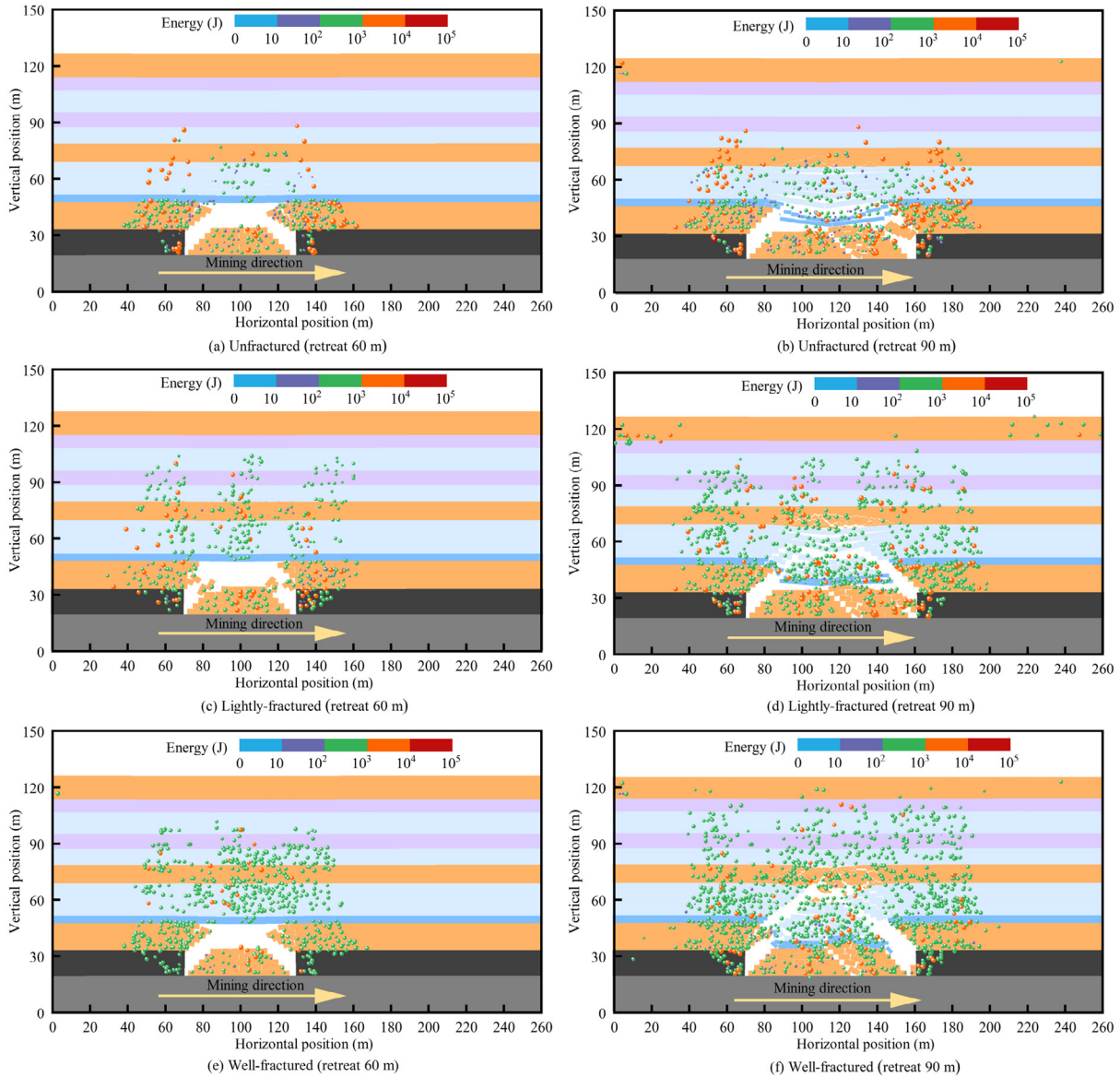


Fig. 17. Distribution characteristics of MS.

After MFHW development, a trend of MS events shifting from lower to higher positions (MFHW for target stratum) was observed through statistical analysis of MS events at different heights, as shown in Fig. 20. Compared to the 401105 longwall, the number of MS events decreased by 34% for the 401106 longwall within the 0–20 m range above the coal seam. However, within the 20–110 m range, the number of MS events increased by 64%.

4. Discussions

4.1. Mechanism of mining-induced stress mitigation

Fracturing the hard strata using MFHW weakens the structural integrity of the roof, causing the initially formed long-distance cantilever of the hard strata roof to converted into a short-distance cantilever [30]. This modification not only reduces the roof bending moment but also diminishes the front abutment pressure in the longwall face. Concurrently, fracturing within rock strata

weakens their structural integrity, leading to a reduced load-bearing capacity of the overlying strata and consequently decreasing the transmission of additional loads.

Numerous studies confirm that coal burst incidents commonly occur due to external dynamic loading superimposed on high static loads [28]. MFHW for the hard strata roof results in a substantial reduction in the periodic roof weighting intensity on the longwall face [31]. This process eliminates the strong dynamic stress caused by massive roof caving and releases mining-induced stress [14,19]. Consequently, this approach alleviates MS events associated with the fracturing for thick, robust rock strata above the gob area of a longwall, ultimately achieving the prevention of coal burst.

After the longwall face retreat, the development of a cantilever structure in the overlying hard roof leads to stress concentration in front of the longwall face, as shown in Fig. 21. Fracturing the hard roof through MFHW shortens the cantilever length and releases some accumulated bending elastic energy. This process achieves depressurization effects and helps mitigate the risk of coal burst. We have established a mechanical model, as depicted in Fig. 22,

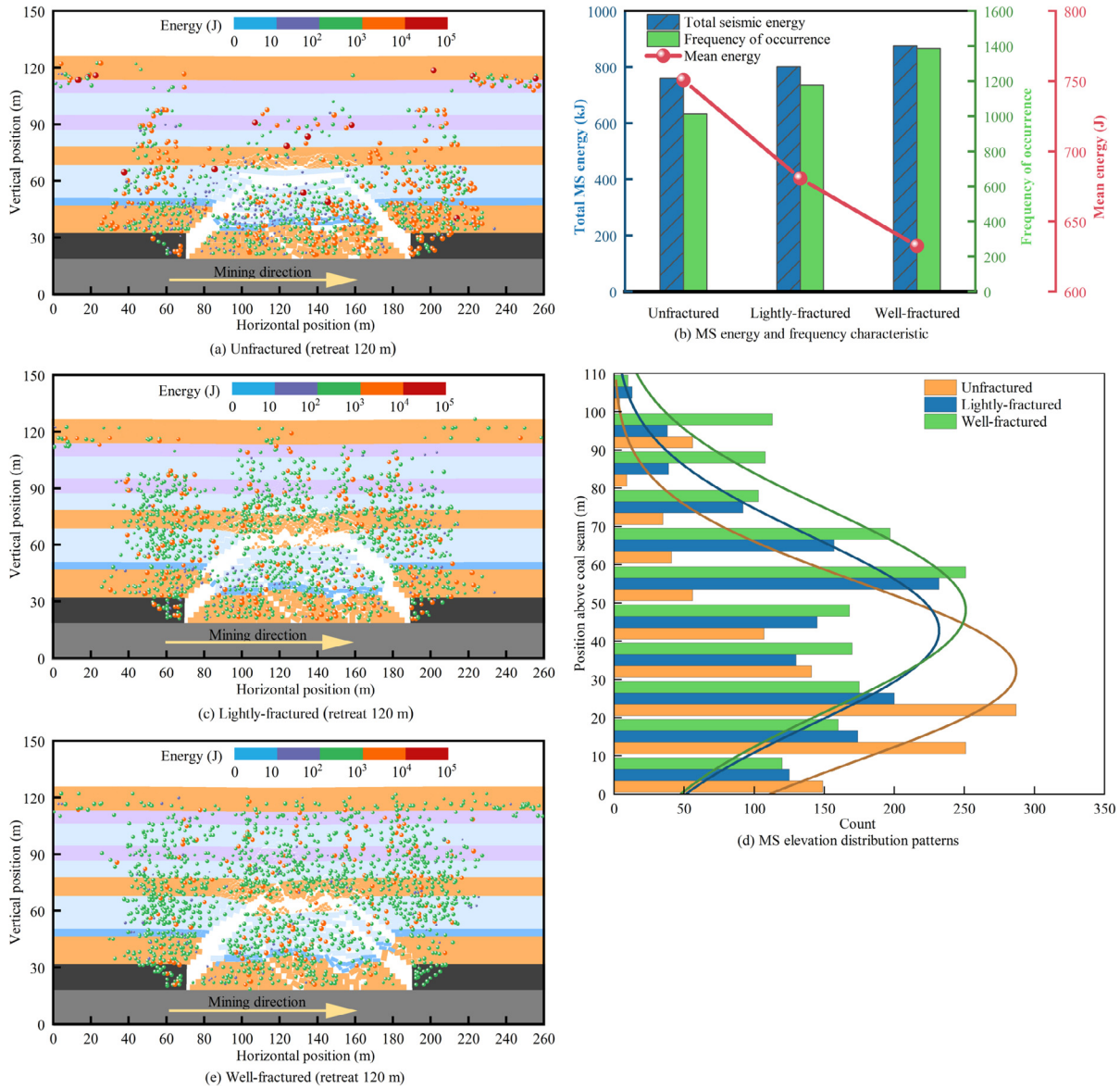


Fig. 18. Statistical overview of MS events during coal mining retreat 120 m.

to analyze the impact of different cantilever lengths on bending elasticity.

We assume that the left side hard roof is the fixed end, while the right side cantilever is above the goaf. We have analyzed the variations in the peak stress position, stress concentration factor, and the area of advanced influence range in front of the working face under different fracturing conditions. Here, L denotes the cantilever length, L_k represents the roof control distance, q_0 signifies the uniformly distributed load and self-weight borne by the hard roof, and q_g denotes the load and self-weight of the cantilever section end hard roof. Field monitoring has revealed that the peak load increment on the hard roof is located several meters in front of the coal wall. This load increment can be simplified as a triangular distribution with aq_0 as the peak load increment, x_0 as the position of the load increment peak relative to the coal wall, x_1 as the distance where the load peak decreases to the elastic zone, p_0 as the support resistance of the strata, M_0 as the bending moment on the roof directly above the coal wall, and Q_0 as the shear force at the same position.

Eq. (7) [32] describes the displacement (y_1) of a semi-infinite elastic foundation beam subjected to the actions of M_0 and Q_0 , within the framework of an elastic foundation beam. The displacement (y_2) caused by the distributed load q on the embedded section of the elastic foundation beam is expressed in Eq. (8).

$$\begin{cases} y_1(x) = 2\beta/k [Q_0\theta(x) + \beta M_0\psi(x)] \\ \theta(x) = e^{-\beta x} \cos \beta x \\ \psi(x) = e^{-\beta x} (\cos \beta x - \sin \beta x) \\ \beta = (k/4EI)^{1/4} \\ I = bh^3/12 \end{cases} \quad (7)$$

where β represents the stiffness ratio, which reflects the ratio of foundation stiffness to the bending stiffness of the hard roof; E the elastic modulus of the hard roof, GPa; I the moment of inertia of the hard roof section, m^4 ; b the width of the hard roof, m; and h the thickness of the hard roof; m.

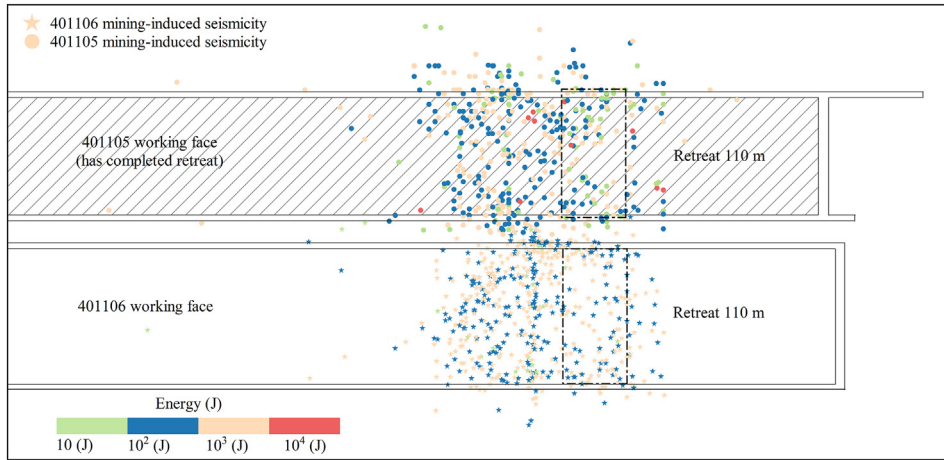


Fig. 19. Location of MS events that occurred during a 110 m advancement of the longwall panel. Note: 401105 working face without MFHW development; 401106 with MFHW development. The dotted black box indicates the 110 m advancement of the longwall panel.

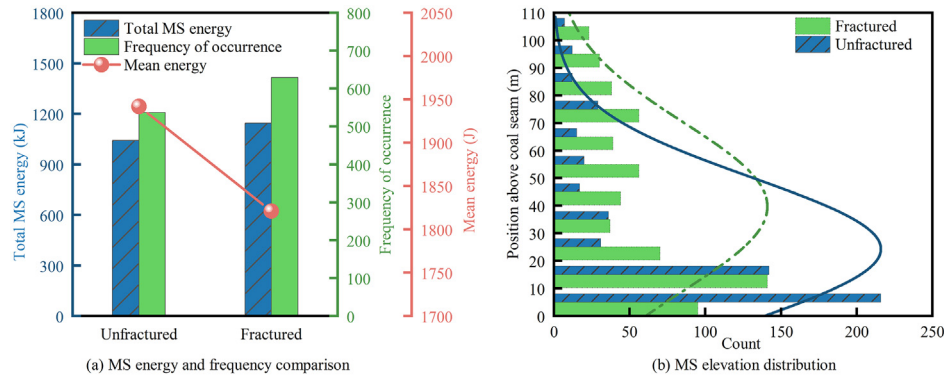


Fig. 20. Comparison of MS activity between the 401106 and 401105 longwall faces.

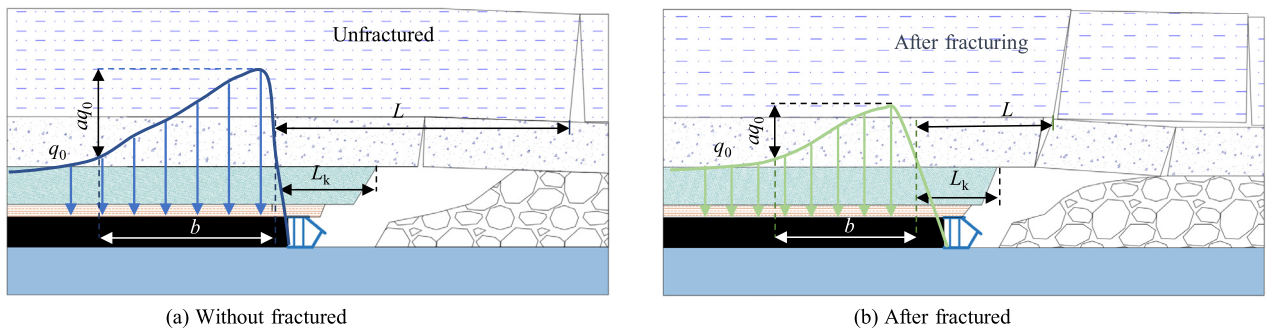


Fig. 21. Load distribution characteristics with or without fractured.

$$\begin{cases}
 y_2(x) = \int_0^x aq_{t1} + \int_x^{x_0} bq_{t1} + \int_0^{x_0} cq_{t1} + \int_{x_0}^x aq_{t2} + \int_x^b bq_{t2} + \int_{x_0}^b cq_{t2} \\
 a = \beta\varphi(x-t)dt/2k \\
 b = \beta\varphi(t-x)dt/2k \\
 c = \beta[\theta(t)\theta(x) + \psi(t)\psi(x)]/2dk \\
 q_{t1} = q_0 + atq_0/x_0 \quad (0 \leq t \leq x_0) \\
 q_{t1} = q_0 + a(b-t)q_0/(b-x_0) \quad (x_0 \leq t \leq b) \\
 \varphi(x) = e^{-\beta x}[\cos(\beta x) + \sin(\beta x)]
 \end{cases}$$

(8)

where t represents the distance of the advanced coal face, m.

A smaller deflection occurs at $x=0$ above the coal wall, which can be regarded as a fixed-end segment. With the constraint conditions for one end fixed, M_0 and Q_0 are calculated by Eq. (9)

$$\begin{cases}
 Q_0 = (q_0 + q_g)L/2 - p_0L_k \\
 M_0 = (q_0/6 + q_g/3)L^2 - p_0L_k^2/4
 \end{cases}$$

(9)

By utilizing $M(x)=Ely''$, the bending moment of the cantilever beam in the pressurized zone can be determined. Using $U(x)$

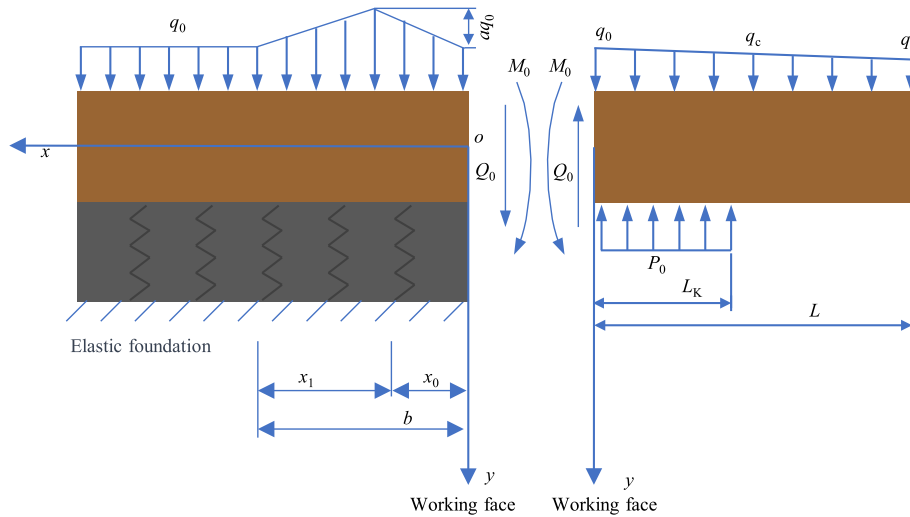


Fig. 22. Force schematic of the hard roof.

$=M^2(x)/2EI$, the strain energy $U(x)$ at the x -section of the rock beam can be calculated.

The study examines how the elastic bending performance of the hard roof strata changes with or without MFHW. Consider the following basic parameters: the elastic foundation stiffness K is 500 MN/m, the thickness of the sandstone layer is 8 m, and the strain modulus of the sandstone layer is 20 GPa. $\beta=0.104$ m, the ahead-of-face influence range $b=60$ m, uniformly distributed load $q_0=15$ MPa, load concentration factor $a=1.5$, distance from the load peak position to the coal wall $x_0=3$ m, load on the cantilever beam segment $q_g=1$ MPa, support load $p_0=0.8$ MPa, and controlling distance $L_k=2$ m.

As depicted in Fig. 23a, after development of MFHW for hard roofs, the length L of the sandstone cantilever decreases, resulting in a decline in the bending elastic energy of the roof. When the cantilever decreases from 20 to 5 m, the maximum value of bending moment decreases from 1549 to 127 MN. As illustrated in Fig. 23b, after MFHW development, the peak stress concentration factor decreases, leading to a reduction in the bending elastic energy of the roof beam. When the stress concentration factor decreases from 3.4 to 1, the maximum value of bending moment decreases from 715 to 237 MN. The energy released from the fracture of the roof beam decreases with MFHW, lowering the risk of coal burst on the longwall face.

4.2. Mechanism of mining-induced seismicity reduction

After the development of MFHW for hard roofs, cracks form within the hard strata roof, causing long beams to become short beams and large blocks to become smaller ones. The prompt rupture of the hard strata roof is beneficial [16]. The strain energy (U) generated during periodic roof stratum breakage is calculated by Eq. (10)

$$U = 3Lq_0^2/10Eh^3 \tag{10}$$

After MFHW development, the hard roof unsupported length (L) decreases, resulting in lower strain energy (U) and reduced dynamic stress associated with mining-induced seismicity during roof rupture. The decrease in hard roof length makes it more prone to collapse. This movement provides space for the overlying strata above the fractured layer, promoting their movement and resulting in more MS events. Due to the decrease in hard roof length, the energy generated by the sliding movement between fractured blocks decreases, as shown in Fig. 24. After MFHW development, as the longwall face retreats, the overlying strata structure (Fig. 24a) transitions to that shown in Fig. 24b above the coal seam. This transition lead to a decrease in the stress exerted on the coal seam, as illustrated in Fig. 16. As a result, the number of MS events

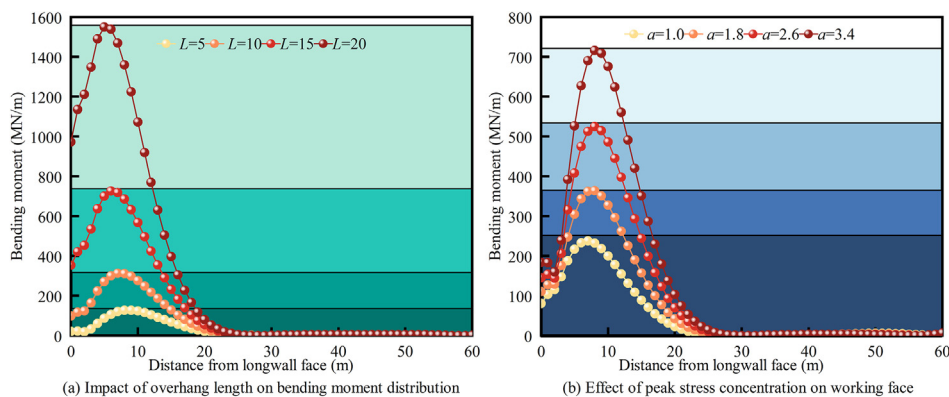


Fig. 23. The influence of fracturing degree on roof bending elasticity.

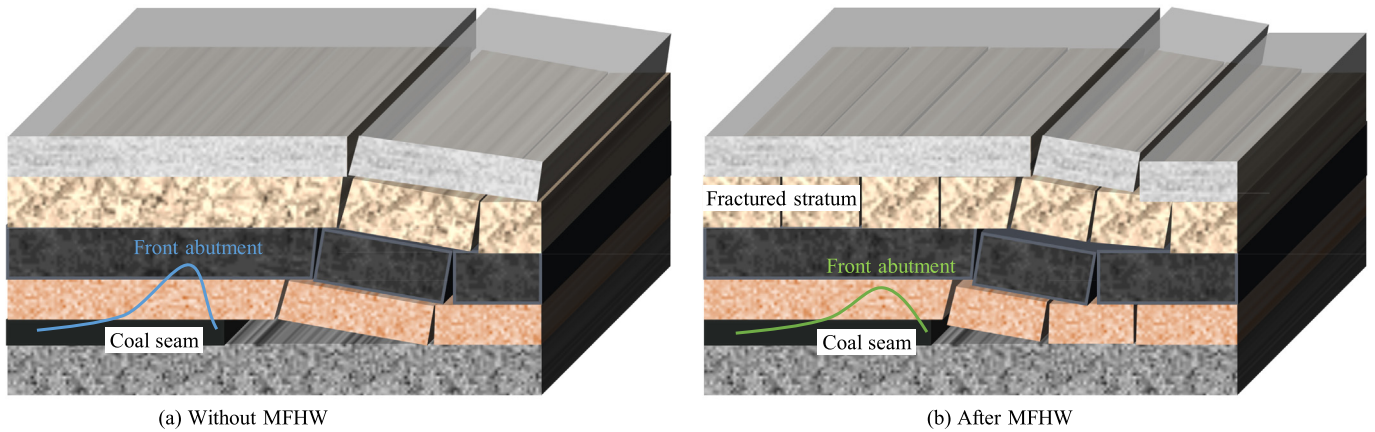


Fig. 24. The influence of fracturing degree on mining-induced seismicity.

in the nearby area of the coal seam decreases. These results align with the trends observed in Fig. 18, where the MS average energy decreased to 680.6 and 632.5 J in lightly and well-fractured conditions, respectively, from 750.7 J in unfractured conditions. Additionally, the frequency of MS events within 0–30 m above the coal seam decreased by 27% and 33% for lightly and well-fractured models, respectively. This reduction in dynamic stress disturbances is advantageous for coal burst control, highlighting the effectiveness of fracturing in mitigating seismic hazards.

4.3. Mechanism of hydraulic fracturing for coal burst control

The underground mining space around the longwall is primarily constituted by three objects: the roof, coal, and floor. The interaction of the roof-coal-floor system essentially controls the coal failure processes. The hard-roof-induced coal burst mechanism model can be depicted as shown in Fig. 25 [28,33]. In this figure, coal was

assumed to exhibit fractured or softened behavior with non-linear characteristics, while the roof and floor were simplified as the surrounding rock and treated as intact material with linear elastic behaviour. The stress behavior of the coal can be described on the right-hand side, while that of the surrounding rock under loading can be depicted on the left. The energy forms involved in the roof-coal-floor system during the entire coal burst process include released elastic energy (U_1) from the surrounding rock, the dissipated energy (U_2) from U_1 , and released energy (U_3) from the roof-coal-floor system. σ_a and σ_b represent the initial stress and residual stress before and after the coal burst, respectively.

Under quasi-static loading (σ_s), when there is a strain increment $\Delta\epsilon_2$ in the coal seam, the corresponding strain increment $\Delta\epsilon_1$ in the surrounding strata of the roof and floor is induced.

$$k_1\Delta\epsilon_1 = k_2\Delta\epsilon_2 \tag{11}$$

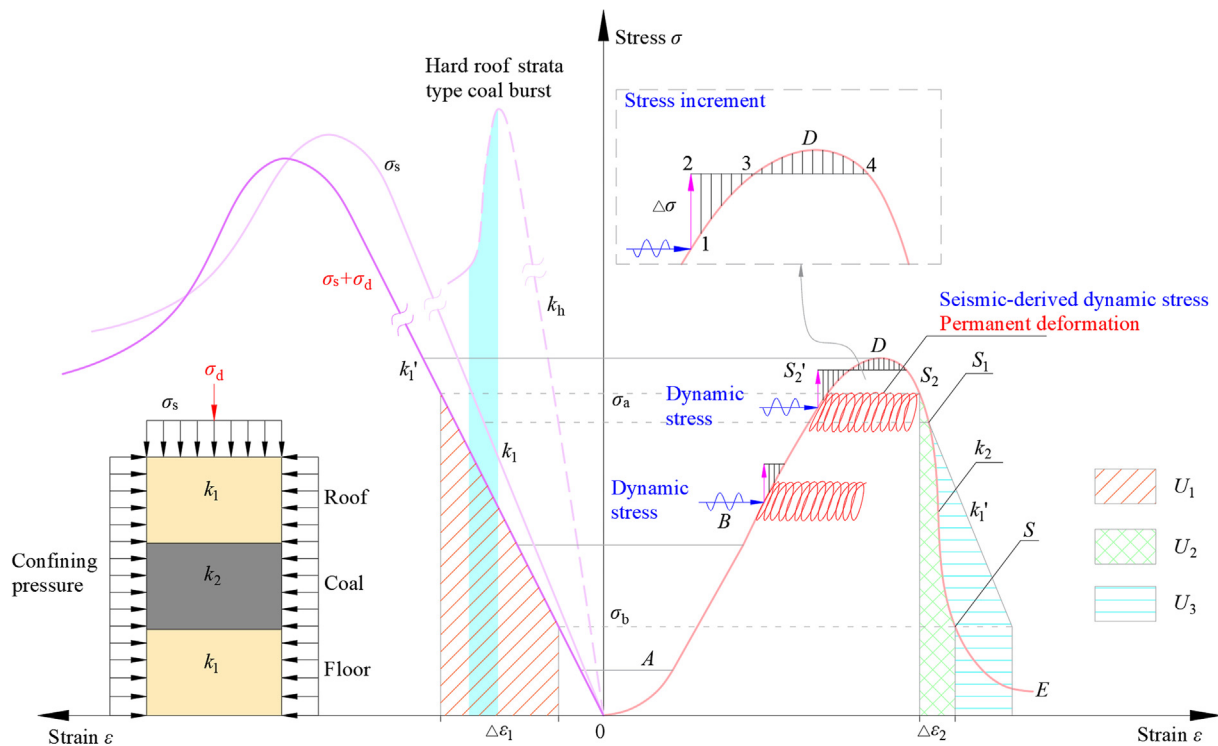


Fig. 25. Schematic diagram of the hard roof-induced coal burst mechanism model.

where k_1 is the elastic modulus of surrounding rock; k_2 the elastic modulus of the coal during unloading; Consequently, the ratio of coal strain ($\Delta\varepsilon_2$) over whole strain ($\Delta\varepsilon$) in the system can be expressed as:

$$\frac{\Delta\varepsilon_2}{\Delta\varepsilon} = \frac{\Delta\varepsilon_2}{\Delta\varepsilon_1 + \Delta\varepsilon_2} = \frac{1}{1 + k_2/k_1} \tag{12}$$

During the occurrence of coal burst, the U_3 can be calculated:

$$U_3 = U_1 - U_2 \approx (k_1 + k_2) \times (\sigma_b^2 - \sigma_a^2) / 2k_1k_2 \tag{13}$$

According to Eq. (12) and Fig. 25, during stage (AB), where $k_1 > 0$ and $k_2 > 0$, the coal-rock system is in the elastic storage stage. Moving to stage (BD), where $k_1 > 0$ and $k_2 > 0$, the surrounding strata of the roof and floor continue to accumulate elastic energy, while the coal begins to undergo plastic deformation, indicating the precursor stage of failure. In stage (DS₁), where $k_2 < 0$ and gradually decreases while k_1 remains constant, $k_1 + k_2 \geq 0$ and $U_3 \leq 0$ at this point. When $k_1 + k_2 = 0$, corresponding to point S₁ in the figure, $\Delta\varepsilon_2/\Delta\varepsilon \rightarrow \infty$, indicating coal burst occurrence. Stage S₁E represents the end of the rock burst process. In hard roof-type coal burst, where the surrounding strata of the hard roof and floor have high strength, the unsupported roof area increases. This implies that $k_1 + k_2$ is significantly greater than 0. Once the hard roof reaches its ultimate strength, the energy released from the failure of the surrounding strata can be enormous, inducing the entire system to undergo a hard roof-type coal burst as illustrated in Fig. 25. Traditional methods (Fig. 26) can be utilized to prevent coal burst. These methods include large diameter borehole [34], borehole

blasting [35], borehole slotting [36], water injection, roof blasting [37], and hydraulic fracturing [9].

The primary objective of these measures is to weaken the roof and floor, which effectively reduces k_1 and decreases the elastic energy storage of the surrounding rock (U_1). As a result, it takes more stress or repeated dynamic stress for the coal mass to reach point D, where potential impact coal burst may happen. On the other hand, measures to weaken the coal mass focus on timely releasing the elastic energy stored in the coal mass, thereby increasing the energy consumption for coal mass failure (U_2). However, the effectiveness of the mentioned methods in preventing coal burst is limited due to several factors. Firstly, these operations require multiple activities along the axial direction of the roadway at different positions, leading to significant manpower consumption. Secondly, the mitigation of mining-induced stress range by these methods is limited. MFHW for hard roofs can significantly weaken the hard roof, reducing k_1 and decreasing both the storage of elastic energy (U_1) in the hard roof and the dynamic stress induced by hard roof collapse.

After the development of MFHW for hard roofs, the hard roof can promptly collapse, restricting the extent of U_1 increase, the stress state of the coal mass tends to remain near point B. This is corroborated by the findings in Fig. 14, where the yy -stress peak ahead of the working face diminishes to 25.4 and 21.7 MPa in the lightly and well-fractured conditions, respectively, compared to 27.2 MPa in the unfractured condition. Additionally, the dynamic stress generated by hard roof is limited, making it difficult to reach point D. This is supported by the findings in Fig. 18, where the average energy of MS events decreased to 680.6 and 632.5 J in lightly and well-fractured conditions, respectively, compared to

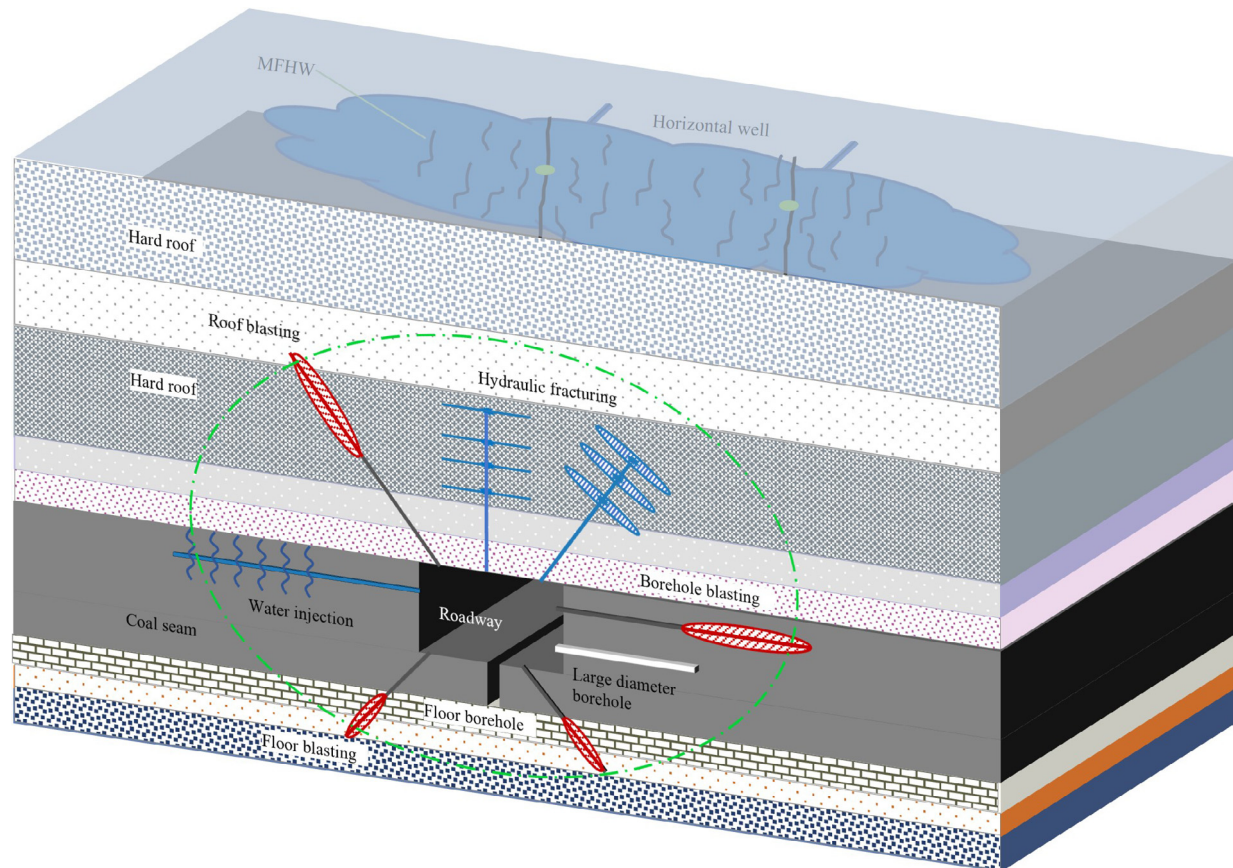


Fig. 26. Prevention strategies of the hard roof-induced coal burst.

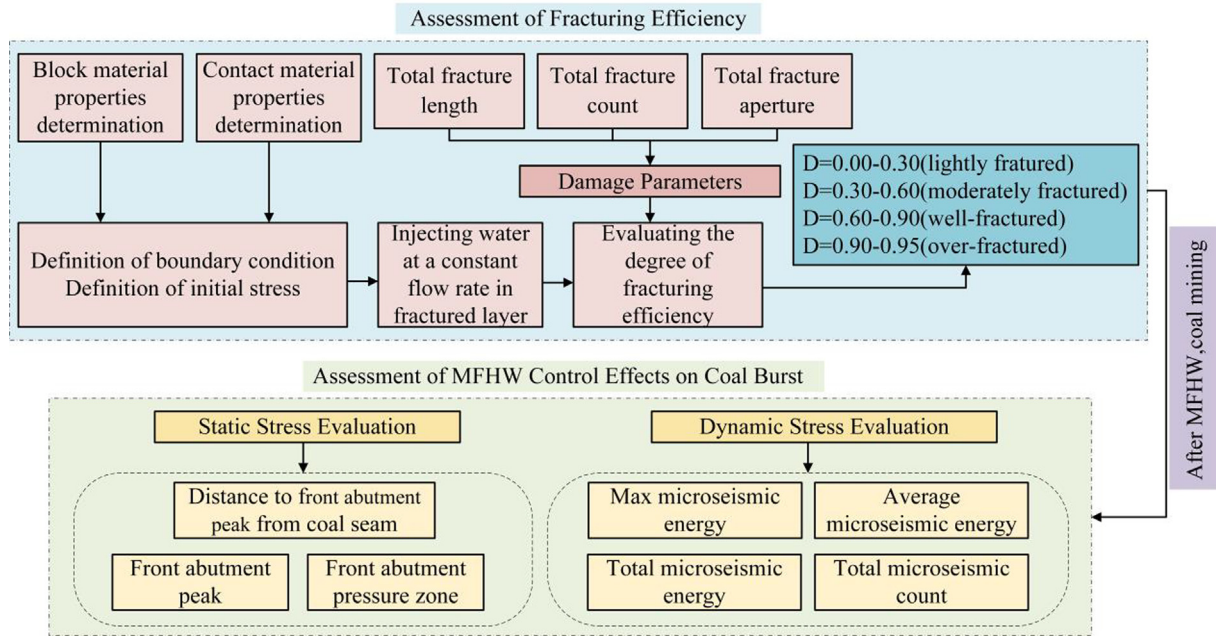


Fig. 27. Flowchart for assessing the effectiveness of MFHW.

Table 3
Evaluation of horizontal multistage hydraulic fracturing effects.

Degree of rock fracturing	Total seismic energy (J)	Total seismic count	Max seismic energy (J)	Average seismic energy (J)	Front-abutment pressure zone (m)	Front-abutment peak (MPa)
Unfractured	759787	1012	38530	750.7	64	26.5
Lightly fractured	801057	1177	20047	680.6	49	24.5
Well-fractured	876004	1385	9937	632.5	32	22.7

750.7 J in unfractured conditions. Moreover, the occurrence frequency of MS events within 0–30 m above the coal seam reduced by 27% and 33% for lightly and well-fractured models, respectively. In summary, the MFHW control mechanisms of coal bursts involve mitigating mining-induced stress and reducing seismic activity during longwall retreat, ensuring stresses remain below the ultimate stress level.

4.4. Assessment of fracturing efficiency and stress mitigation

Fig. 27 illustrates the process flowchart for evaluating the effectiveness of MFHW. Initially, a numerical model is established using the actual rock mechanics parameters and prevailing stress conditions of the mine. Hydraulic fracturing is then simulated in the numerical model, corresponding to the actual water injection locations in the horizontal well. The FISH function is used to quantify the total number, length, and aperture of fractures during the water injection process. Based on these fracture characteristics, the degree of fracturing in the target layer is calculated using the methodology described in Ref [28]. This assessment enables the determination of the required water injection volume for achieving different degrees of fracturing. After the developing MFHW for hard roofs, coal seam retreat begins, allowing for the evaluation of its effectiveness in preventing coal burst. A quantitative assessment of the MFHW effects is summarized in Table 3.

In terms of dynamic stress, the model calculates the total number of MS events, total energy, maximum energy, and average energy during the mining-induced seismicity process. For static stress, parameters such as the influence range of front abutment pressure, peak front abutment pressure, and distance from the coal wall where the peak front abutment pressure occurs are calculated. Finally, a comparative analysis is conducted to examine changes in indicators related to dynamic and static stress. This analysis compares the conditions under different degree of fracturing to the unfractured condition. The aim is to pre-assess the efficacy of hydraulic fracturing in the hard roof strata for improving stress conditions during longwall face retreat.

5. Conclusions

This paper reproduces the process by which MFHW reduces mining-induced stress and high-energy seismic events, using both simulation and field data analysis. The MFHW control mechanisms of coal burst is discussed. The main conclusions are as follows:

- (1) The MFHW control mechanisms of coal burst involve mitigating mining-induced stress and reducing mining-induced seismic during the longwall retreat process, ensuring these stresses fall below the ultimate stress level. This reduction in stress and seismic activity decreases the likelihood of coal

burst development. Additionally, the effectiveness of MFHW fracturing can be assessed through the parameter D , while the coal burst control effectiveness is evaluated using static-dynamic stress analysis. It has been established how the degree of fracturing influences the improvement in the stress environment during longwall mining.

- (2) The study introduces a classification system for the degree of roof fracturing based on the total number, length, and aperture of fractures generated during the MFHW process. The fracturing degrees are classified as lightly fractured ($D \leq 0.3$), moderately fractured ($0.3 < D \leq 0.6$), well-fractured ($0.6 < D \leq 0.9$), and over-fractured ($0.9 < D \leq 0.95$). A response stage in the fracturing process, characterized by a slowdown in crack development, indicates the transition to a well-fractured condition.
- (3) The implementation of MFHW leads to an increase in the number of MS events, with total frequency and energy release increasing, while the average energy per event decreases. Specifically, events corresponding to the 10 , 10^3 , and 10^4 J decrease, whereas the 10^2 J events increase. Within the range of 0–30 m above the coal seam, the quantity of MS events decreases, whereas in the range of 30–100 m, the quantity of events increases. Compared to the unfractured scenario, both lightly and well-fractured scenarios resulted in increased total mining-induced seismic energy by 5% and 15%, and total frequency by 16% and 37%, respectively. Meanwhile, average mining-induced seismic energy decreased by 9% and 16%, respectively.
- (4) Hydraulic fracturing significantly weakens the structural integrity of the hard roof, facilitating its prompt collapse and reducing additional loading caused by the overhanging structure. This collapse leads to a reduction in the front-abutment pressure zone and a decrease in the front-abutment peak. Additionally, it increases the distance between the front-abutment pressure peak and the coal wall. Compared to the scenario without fractured, both lightly and well-fractured scenarios resulted in reductions of 7.5%, 14.3%, 23%, and 50% in the front-abutment peak and pressure zone, respectively.

Acknowledgments

The authors sincerely thank Qiang Lu and Yuanjian Qiu for their invaluable assistances in data processing and analysis. We gratefully acknowledge the financial support for this work provided by the National Natural Science Foundation of China (Nos. 52274147, 52374101, and 32111530138), the Jiangsu Province Basic Research Special Fund-Soft Science Research (No. BZ2024024), and the State Key Research Development Program of China (No. 2022YFC3004603).

References

- [1] Kaiser PK, Cai M. Design of rock support system under rockburst condition. *J Rock Mech Geotech Eng* 2012;4(3):215–27.
- [2] Xu LM, Lu KX, Pan YS, Qin ZJ. Study on rock burst characteristics of coal mine roadway in China. *Energy Sources Part A Recovery Util Environ Eff* 2022;44(2):3016–35.
- [3] Wang GF, Gong SY, Dou LM, Cai W, Jin F, Fan CJ. Behaviour and bursting failure of roadways based on a pendulum impact test facility. *Tunn Undergr Space Technol* 2019;92:103042.
- [4] Wang W, Cheng YP, Wang HF, Liu HY, Wang L, Li W, Jiang JY. Fracture failure analysis of hard-thick sandstone roof and its controlling effect on gas emission in underground ultra-thick coal extraction. *Eng Fail Anal* 2015;54:150–62.
- [5] Ma Q, Liu XL, Tan YL, Wang RS, Xie WQ, Wang EZ, Liu X, Shang J. Experimental study of loading system stiffness effects on mechanical characteristics and kinetic energy calculation of coal specimens. *Rock Mech Rock Eng* 2024.
- [6] Yu ML, Zuo JP, Sun YJ, Mi CN, Li ZD. Investigation on fracture models and ground pressure distribution of thick hard rock strata including weak interlayer. *Int J Min Sci Technol* 2022;32(1):137–53.
- [7] He J, Dou LM, Mu ZL, Cao AY, Gong SY. Numerical simulation study on hard-thick roof inducing rock burst in coal mine. *J Cent South Univ* 2016;23(9):2314–20.
- [8] Huang BX, Wang YZ. Roof weakening of hydraulic fracturing for control of hanging roof in the face end of high gassy coal longwall mining: A case study. *Arch Min Sci* 2016;61(3):601–15.
- [9] He H, Dou LM, Fan J, Du TT, Sun XL. Deep-hole directional fracturing of thick hard roof for rockburst prevention. *Tunn Undergr Space Technol* 2012;32:34–43.
- [10] Yu H, Xu WL, Li B, Huang HW, Micheal M, Wang Q, Huang MC, Meng SW, Liu H, Wu HA. Hydraulic fracturing and enhanced recovery in shale reservoirs: Theoretical analysis to engineering applications. *Energy Fuels* 2023;37(14):9956–97.
- [11] Vishkai M, Gates I. On multistage hydraulic fracturing in tight gas reservoirs: Montney Formation, Alberta, Canada. *J Petrol Sci Eng* 2019;174:1127–41.
- [12] Masum SA, Chen M, Hosking LJ, Stańczyk K, Kapusta K, Thomas HR. A numerical modelling study to support design of an *in situ* CO₂ injection test facility using horizontal injection well in a shallow-depth coal seam. *Int J Greenh Gas Contr* 2022;119:103725.
- [13] Kang HP, Lv HW, Gao FQ, Meng XZ, Feng YJ. Understanding mechanisms of destressing mining-induced stresses using hydraulic fracturing. *Int J Coal Geol* 2018;196:19–28.
- [14] Yu B, Gao R, Kuang TJ, Huo BJ, Meng XB. Engineering study on fracturing high-level hard rock strata by ground hydraulic action. *Tunn Undergr Space Technol* 2019;86:156–64.
- [15] Zhu JZ, Li WP, Teng B, Liu Y. Failure characteristics of thick hard roof stratum under hydraulic pre-splitting and its application in a coal mine, Dongsheng mining area. *Environ Earth Sci* 2024;83(6):153.
- [16] Jendryś M, Hadam A, Cwiękała M. Directional hydraulic fracturing (DHF) of the roof, as an element of rock burst prevention in the light of underground observations and numerical modelling. *Energies* 2021;14(3):562.
- [17] Liu JW, Liu CY, Yao QL, Si GY. The position of hydraulic fracturing to initiate vertical fractures in hard hanging roof for stress relief. *Int J Rock Mech Min Sci* 2020;132:104328.
- [18] Pan C, Xia BW, Yu B, Yu P, Luo YF, Gao YG. Determination of the key parameters of high-position hard roofs for vertical-well stratified fracturing to release strong ground pressure behavior in extra-thick coal seam mining. *Energy Sci & Eng* 2020;8(6):2216–38.
- [19] Liang YB, Cheng YF, Han ZY, Yan CL, Liu ZH, Zhang XF, Wang C. Study on control of dynamic disaster induced by high-level ETHR fracture by ground fracturing. *Acta Geophys* 2023;71(3):1273–87.
- [20] Qian YN, Li QG, Jiang ZZ, Hu QT, Wu WB, Liu Y, Li L, Zhang Z, Yu C, Li W. Microseismic activity characteristics and range evaluation of hydraulic fracturing in coal seam. *Gas Sci Eng* 2024;122:205222.
- [21] Cundall PA. A computer model for simulating progressive large-scale movements in blocky rock systems. *Proceedings Symp Int Soc Rock Mech Nancy 2* 1971(1):11–18.
- [22] Wang J, Xie HP, Matthai SK, Hu JJ, Li CB. The role of natural fracture activation in hydraulic fracturing for deep unconventional geo-energy reservoir stimulation. *Petrol Sci* 2023;20(4):2141–64.
- [23] Hubbert MK, Willis DG. Mechanics of hydraulic fracturing. *Trans AIME* 1957;210(1):153–68.
- [24] Cao JR, Dou LM, He J, Xie JH, Han ZP, Wang SW. Mechanism of the coal bursts in the working face during mining of steeply inclined and extra thick coal seam. *Geomat Nat Hazards Risk* 2023;14(1):2206511.
- [25] Gao FQ, Stead D, Coggan J. Evaluation of coal longwall caving characteristics using an innovative UDEC Trigon approach. *Comput Geotech* 2014;55:448–60.
- [26] Wang JC, Li M, Wang ZH, Li Z, Zhang H, Song SX. The influence of inter-band rock on rib spalling in longwall panel with large mining height. *Int J Min Sci Technol* 2024;34(4):427–42.
- [27] Li N, Fang LL, Sun WC, Zhang X, Chen D. Evaluation of borehole hydraulic fracturing in coal seam using the microseismic monitoring method. *Rock Mech Rock Eng* 2021;54(2):607–25.
- [28] Cai W, Bai XX, Si GY, Cao WZ, Gong SY, Dou LM. A monitoring investigation into rock burst mechanism based on the coupled theory of static and dynamic stresses. *Rock Mech Rock Eng* 2020;53(12):5451–71.
- [29] Zhou HW, Lu MY, Xie HP, Jia WH, Peng RD, Wang YM, Chen B, Jing P. Numerical analysis on mechanical difference of sandstone under *in situ* stress, pore pressure preserved environment at depth. *Int J Min Sci Technol* 2023;33(11):1339–50.
- [30] Liu ZH, Wang SH, Ye HL, Yang LS, Feng F, Lian HJ, Yang D. Experimental study on the effects of pre-cracks, fracturing fluid, and rock mechanical characteristics on directional hydraulic fracturing with axial pre-cracks. *Geomech Geophys Geo Energy Geo Resour* 2021;7(2):29.

- [31] Sun YX, Fu YK, Wang T. Field application of directional hydraulic fracturing technology for controlling thick hard roof: A case study. *Arab J Geosci* 2021;14(6):438.
- [32] Feng LF, Dou LM, Wang XD, Jin DW, Cai W, Xu GG, Jiao B. Mechanism of mining advance speed on energy release from hard roof movement. *J China Coal Soc* 2019; 44(11): 3329-39.
- [33] Cai W, Dou L, Si G, Hu Y. Fault-Induced Coal Burst Mechanism under Mining-Induced Static and Dynamic Stresses. *Engineering* 2021;7(5):687–700.
- [34] Cao AY, Dou LM, Cai W, Gong SY, Liu S, Jing GC. Case study of seismic hazard assessment in underground coal mining using passive tomography. *Int J Rock Mech Min Sci* 2015;78:1–9.
- [35] Konicek P, Soucek K, Stas L, Singh R. Long-hole destress blasting for rockburst control during deep underground coal mining. *Int J Rock Mech Min Sci* 2013;61:141–53.
- [36] Si GY, Durucan S, Shi JQ, Korre A, Cao WZ. Parametric analysis of slotting operation induced failure zones to stimulate low permeability coal seams. *Rock Mech Rock Eng* 2019;52(1):163–82.
- [37] He MC, Wang Q. Rock dynamics in deep mining. *Int J Min Sci Technol* 2023;33(9):1065–82.